

# Modeling and predicting the shape of the far-infrared/submillimeter emission in ultra-compact HII regions and cold clumps

D. Paradis<sup>1,2</sup>, C. Mény<sup>1,2</sup>, A. Noriega-Crespo<sup>3,6</sup>, R. Paladini<sup>3</sup>, J.-P. Bernard<sup>1,2</sup>, C. Bot<sup>4</sup>, L. Cambrésy<sup>4</sup>, K. Demyk<sup>1,2</sup>, V. Gromov<sup>5</sup>, A. Rivera-Ingraham<sup>1,2</sup>, and M. Veneziani<sup>3</sup>

<sup>1</sup> Université de Toulouse; UPS-OMP; IRAP; Toulouse, France

<sup>2</sup> CNRS; IRAP; 9 Av. du Colonel Roche, BP 44346, F-31028, Toulouse, cedex 4, France

<sup>3</sup> Spitzer Science Center, California Institute of Technology, 1200 E. California Blvd, Pasadena, CA 91125, USA

<sup>4</sup> Observatoire astronomique de Strasbourg, Université de Strasbourg, CNRS, UMR 7750, 11 rue de l'Université, 67000 Strasbourg, France

<sup>5</sup> Space Research Institute, RAS, 84/32 Profsoyuznaya, 117810 Moscow, Russia

<sup>6</sup> Space Telescope Science Institute, 3700 San Martin Dr, Baltimore, MD, 21218, USA

## ABSTRACT

**Context.** Dust properties are likely affected by the environment in which dust grains evolve. For instance, some analyses of cold clumps (7 K- 17 K) lead to favor the aggregation process in dense environments. However, the study of warm (30 K-40 K) dust emission at long wavelength ( $\lambda > 300 \mu\text{m}$ ) has been limited by the difficulty in combining far infrared-millimeter (FIR-mm) spectral coverage and high angular resolution to observe warm dust grains.

**Aims.** Using Herschel data from 70 to 500  $\mu\text{m}$ , as part of the Herschel infrared Galactic (Hi-GAL) survey associated to 1.1 mm data from the Bolocam Galactic Plane Survey (BGPS), we compare emission in two types of environments: ultra-compact HII (UCHII) regions and cold molecular clumps (denoted as cold clumps). This comparison allows us to test models of dust emission in the FIR-mm domain used to reproduce emission in the diffuse medium, in these environments, and to check their ability to predict the dust emission in our Galaxy.

**Methods.** We determine the emission spectra in twelve UCHII regions and twelve cold clumps, and derive the dust temperature ( $T$ ) using the recent two-level system (TLS) model with three sets of parameters, and the so-called  $T\text{-}\beta$  (Temperature-dust emissivity index) phenomenological models, with  $\beta$  set up to 1.5, 2 and 2.5.

**Results.** The applicability of the TLS model in warm regions has been tested for the first time. This analysis points out distinct trends in the dust emission between cold and warm environments, visible through changes in the dust emissivity index. However, with the use of standard parameters, the TLS model is able to reproduce the spectral behavior observed in cold and warm regions, by the only change of the dust temperature, as opposed to a  $T\text{-}\beta$  model which requires the knowledge of  $\beta$ .

**Key words.** ISM:dust, extinction - Infrared: ISM - Submillimeter: ISM

## 1. Introduction

The study of the extended far-infrared (FIR) and submillimeter (submm) sky emission is a relatively young subject. This wavelength range is dominated by emission from large (15 to 100 nm) silicate-based interstellar grains (also called big grains or BG), that dominate the total dust mass and radiate at thermal equilibrium with the surrounding radiation field. The FIR/submm emission is routinely used to infer total gas column density and mass of objects ranging from molecular clouds to entire external galaxies, assuming that dust faithfully traces the gas. In the past (before the 2000s), in the absence of sufficient observational data, the emission was expected to follow, assuming optically thin medium and a single dust temperature along the line of sight, the so-called  $T\text{-}\beta$  model:

$$I_\nu(\lambda) = \epsilon(\lambda_0) \left( \frac{\lambda}{\lambda_0} \right)^{-\beta} B_\nu(\lambda, T) N_H = Q_{abs}(\lambda) B_\nu(\lambda, T) N_H, \quad (1)$$

with  $\beta=2$ .  $I_\nu$  is the sky brightness,  $\epsilon(\lambda_0)$  is the emissivity at the reference wavelength  $\lambda_0$ ,  $B_\nu$  is the Planck function,  $T$  is the thermal dust temperature,  $N_H$  is the hydrogen column density, and  $Q_{abs}$  is the absorption efficiency. Such  $T\text{-}\beta$  model with  $\beta=2$  is the correct asymptotic behavior (towards long wavelengths)

of the Lorentz model (the well-known and successful physical model for bound oscillators). The Lorentz model describes the mid-IR vibrational bands of the silicate-based interstellar grains.

Balloon (PRONAOS, Archeops) and satellite (FIRAS, WMAP) mission have measured the extended interstellar emission in various photometric FIR/submm/mm bands. These data analyses have revealed that the FIR/submm emission cannot be explained by a simple extrapolation of the mid-IR emission. Since these observations, the FIR/submm emission is often modeled with the  $T\text{-}\beta$  model, with  $\beta$  taken as a free parameter, mainly in the range 1 to 3. This model, with a constant  $\beta$  from FIR to submm and different from 2, became an empirical model, which can consequently hide any possible more complex dependences of the emissivity with wavelength and temperature. It has been observed that:

- Indeed, the observed FIR/submm dust emissivity ( $\epsilon(\lambda)$ ) appears to have a more complex dependence with wavelength than described by the  $T\text{-}\beta$  model: the emission spectrum flattens in the submillimeter as compared to a modified black-body emission with  $\beta = 2$  (Reach et al., 1995; Finkbeiner et al., 1999; Galliano et al., 2005; Paladini et al., 2007; Paradis et al., 2009, 2011). This has led to an empirical change in the optical con-

stants of the Draine’s astro-silicates (Draine & Lee, 1984) for wavelengths larger than 250  $\mu\text{m}$  (Li & Draine, 2001).

- The dust emissivity appears to be temperature-dependent, the emissivity spectra being flatter with increasing dust temperature (Dupac et al., 2003; Désert et al., 2008; Veneziani et al., 2010). When the dust emission is modelled with the usual T- $\beta$  model, a degeneracy between T and  $\beta$  parameters has been highlighted by the various methods of data fitting ( $\chi^2$ , hierarchical Bayesian, ... ). Therefore, noise can move the optimal solution (decreasing T and increasing  $\beta$ , or vice versa). However, a systematic anti-correlation of  $\beta$  with temperature is claimed to persist (Juvella et al., 2013). Similar variations of  $\beta$  with temperature are seen in laboratory spectroscopic experiments on amorphous dust analogs (Mennella et al., 1998; Boudet et al., 2005; Coupeaud et al., 2011).

These preliminary results have been confirmed using Herschel photometric data (Paradis et al., 2012, 2010) as part of the Hi-GAL survey, an Herschel open time Key-project (PI S. Molinari) that mapped the entire Galactic Plane (GP) of our Galaxy (Molinari et al., 2010a,b). In the Herschel wavelength range, dust emissivity spectral variations are often identified with a 500  $\mu\text{m}$  emission excess (Gordon et al., 2010; Galliano et al., 2011; Paradis et al., 2012). In the Large Magellanic Cloud, this excess has been shown to correlate with temperature and to anti-correlate with brightness (Galliano et al., 2011). A similar behaviour is found along the GP using Hi-GAL photometric data where a significant 500  $\mu\text{m}$  excess is observed towards the peripheral regions of the GP ( $35^\circ < l < 70^\circ$ ), and can reach up to 16-20% of the emissivity (see Paradis et al., 2012, Figure 1, panel A). The excess is often maximum (>25%) toward HII regions, but it does not appear to be a systematic behavior. However, the Herschel spectral coverage is limited to 500  $\mu\text{m}$ .

Dust emission and dust processes occurring in warm/hot environments such as ultra-compact HII (UCHII) regions are poorly known in the FIR/submm wavelength range. These regions are some of the most luminous objects in the Galaxy at FIR wavelengths, with dust temperatures up to 80 K, and are ideal targets to look for warm/hot dust emission. HII regions correspond to photoionized regions surrounding O and B stars. UCHII regions are small (linear size below 0.1 pc) and dense (electronic density  $n_e > 10^4 \text{ cm}^{-3}$ ), with O and B stars newly formed, before the ionized gas extends to become compact HII regions. They have been identified using the IRAS Point Source Catalog (PSC), based on the [25-12] and [60-12] colors (Wood & Churchwell, 1989a). UCHII regions, have various properties (size, brightness temperature) and morphologies (cometary, spherical, core-halo, arc-like, shell, or more complex, see Peeters et al., 2002), significantly different from the standard Stromgren sphere model (Wood & Churchwell, 1989b), depending on the complex interaction of hot stars and their natal molecular cloud. The different morphologies of the UCHII regions come from the ambient medium surrounding the star, but also from the strong stellar winds of the O and B stars, creating a cavity in the ionized gas, or from the motion of the star through the cold molecular gas. All these conditions might certainly affect dust properties inside the UCHII regions. Grain destruction/fracturing could take place in UCHII regions. Also, the radiation field could potentially modify the grain surface, that could change the dust emissivity.

On the opposite temperature regime, cold clumps, associated to molecular clouds, evidence dust emitting at temperatures between  $\sim 7$  K and  $\sim 17$  K. Analyses of cold cores allow us to

**Table 1.** Galactic coordinates (in degree) of the selected UCHII regions and cold clumps.

Regions	GLON	GLAT
IRAS 17279-3350	354.204	-0.036
IRAS 17455-2800	1.126	-0.109
IRAS 17577-2320	6.554	-0.098
IRAS 18032-2032	9.620	0.197
IRAS 18116-1646	13.873	0.282
IRAS 18317-0757	23.954	0.150
IRAS 18434-0242	29.955	-0.014
IRAS 18469-0132	31.395	-0.255
IRAS 18479-0005	32.795	0.192
IRAS 18502+0051	33.914	0.109
IRAS 19442+2427	60.885	-0.129
IRAS 19446+2505	61.477	0.091
Cold Clump-1	17.923	-0.006
Cold Clump-2	17.964	0.079
Cold Clump-3	18.314	0.035
Cold Clump-4	18.104	0.379
Cold Clump-5	18.349	-0.273
Cold Clump-6	18.411	-0.291
Cold Clump-7	18.572	-0.431
Cold Clump-8	18.559	-0.153
Cold Clump-9	30.006	-0.270
Cold Clump-10	41.715	0.035
Cold Clump-11	42.874	-0.180
Cold Clump-12	52.342	0.324

study the initial phases of star formation, i. e. the pre-stellar core fragmentation. In the past (before Planck and Herschel observations), these objects were poorly detected in surveys covering wavelengths below 200  $\mu\text{m}$  because of their low temperatures and weak emission. Some of them were, however, already studied in the submm and mm domain with ground-based facilities. Recently,  $\approx 10000$  cold clumps have been cataloged using Planck data (Planck Collaboration, 2011), and some of them were observed with Herschel, in specific programs. Their emission spectra point out high dust emissivity index, sometimes as high as 3.5. This observed behavior could result from grain coagulation in dense and cold environments (Stepnik et al., 2003; Paradis et al., 2009; Kohler et al., 2011, 2012).

Although FIR/mm emission is usually modeled with a modified black body, an alternative model has been developed by Mény et al. (2007), referred as the two-level system (TLS) model, in the following. It is a physical model for silicate BG emission in the FIR/mm range, derived from solid state modeling of general optical properties of the dielectric amorphous state. This model is qualitatively in agreement with laboratory experiments on amorphous silicates, and is coherent with some observational facts, such as the flattening of the emission at long wavelengths. It is also compatible with some observations in the amplitude of this flattening in the Galactic plane observed with Herschel data (Paradis et al., 2012). Without excluding other effects like temperature distributions along the line of sight, grain aggregations, carbon layers on silicate-based grains, it is important to interpret the observations in terms of emission of dielectric grains (silicate maybe mixed with ice) radiating at a single temperature along the line of sight. The observations can be modeled with the four free parameters of the TLS model (Paradis et al., 2011) allowing us to reproduce the Galactic diffuse medium (denoted in the following as

diffuse parameters), Galactic compact sources (denoted as compact sources parameters) and both environments (denoted as standard parameters). A full understanding of the observed dust emission would require a detailed analysis including radiative transfert, a distribution of grain sizes, a description of the morphology (aggregation, ice mantles, ...) of the grains, and the true IR/FIR/mm properties of the various materials that are present in the grain distribution (various silicates, ices and carbon types, with some control on their degree of amorphisation, hydrogenation, ...). We note that some tests on temperature mixing along the line of sight in the inner Galactic plane have been performed in Paradis et al. (2012). In this work the authors showed that the changes in the observed emissivity spectra with dust temperature could not be accounted for by a line of sight effect only, but could result instead from intrinsic variations in the dust properties with environment.

Most studies in the FIR/mm domain require a realistic determination of dust temperature and dust column density over large parts of the sky. This is of primary importance to predict emission intensity at any other FIR/mm wavelengths, to determine masses, to remove some Galactic foregrounds components from cosmological signals (such as CMB) which requires very accurate extrapolation in frequency, or to evidence variations in the general dust emission properties in various environments. Therefore, understanding variations in dust emissivity is primordial. The aim of this work is to compare the shape of the dust emission in different environments in order to investigate if distinct properties can be pointed out, and if so, to be able to accurately reproduce the shape of dust emission spectra in connection with the environment. However, we also want to be able to easily predict dust emission in any regions of our Galaxy, even when the characteristics of the region, i. e. types of the environment (diffuse, cold, warm) for instance, are unknown. We compare the ability of the TLS model with the three sets of parameters (diffuse, compact sources, standard), as well as a T- $\beta$  model with three fixed values of  $\beta$  (1.5, 2 and 2.5) to fit the BG emission in warm and cold regions of the Galactic interstellar medium.

The main goal of this work is to investigate the potentially distinct dust properties according to the environment and to be able to predict the FIR to mm emission in cold and warm regions. In this study, we combine Bolocam with Herschel data to extend the spectral coverage to mm wavelengths (1.1 mm), important to detect any changes in the shape of the emission spectrum. MSX (Midcourse Space Experiment) data in band E (21.3  $\mu\text{m}$ ) and Spitzer data at 24  $\mu\text{m}$  are also presented but not included in the modeling. In section 2 we give a brief summary of the surveys used here, then in Section 3, we explain the selection of targets in the two specific environments we focused on (UCHII regions and cold clumps). Description of the method (including dust emission extraction and modeling) is given in Section 4. Discussions and conclusions are provided in Sections 5 and 6, respectively.

## 2. Data

### 2.1. Hi-GAL survey

The Hi-GAL survey covers the entire Galactic plane ( $-1^\circ < b < +1^\circ$ ), at five wavelengths (70, 160, 250, 350 and 500  $\mu\text{m}$ ), with an angular resolution going from 6'' to 37''. The processing of the data was performed using the ROMAGAL software (Traficante et al., 2011). The PACS and SPIRE absolute zero level were calibrated applying gains and offsets derived

from the comparison to the Planck-High Frequency Instrument and IRIS (Improved Reprocessing of the IRAS Survey, see Miville-Deschênes & Lagache, 2005) data (see Bernard et al., 2010; Paradis et al., 2012).

### 2.2. BGPS survey

With an angular resolution of 33'', the Bolocam Galactic Plane Survey (BGPS, Aguirre et al., 2011) covers the longitude and latitude ranges  $-10.5^\circ \leq l \leq 90.5^\circ$ ,  $|b| \leq 0.5^\circ$ , in a contiguous way. Extensions in latitude have been performed in some regions (Cygnus X spiral arm,  $l=3^\circ, 15^\circ, 30^\circ$  and  $31^\circ$ ). Four regions in the outer Galaxy have also been observed: IC1396, a region towards the Perseus arm, W3/4/5 and Gem OB1. The total area of the coverage is 170 square degrees. A full description of the BGPS can be found in Aguirre et al. (2011). Data, in unit of Jy/beam, have first been converted into MJy/sr using eq. 16 from Aguirre et al. (2011), derived from the beam surface value. We use the new version of the data (v2.0), delivered beginning of 2013. In this version, data do not suffer from calibration issues anymore, i. e. the 1.5 factor needed by the latter authors in the previous version of the data, to obtain consistency with other data sets, has been understood and solved. However, the processing of the maps could attenuate by 50% the aperture flux for structures extending to 3.8'.

### 2.3. Additional data

Near-infrared (NIR) data such as the MSX data in Band E (21.3  $\mu\text{m}$ , with a resolution of 20'') and Spitzer data (24  $\mu\text{m}$ , with a resolution of 6'') as part of the MIPS GAL program (PI: S. Carey, Carey et al., 2009) have also been analyzed, in cases of UCHII regions, but not included in any modeling (see Section 4.2). Most of the UCHII regions we are interested in are very bright and some pixels of the 24  $\mu\text{m}$  images were saturated. Those pixels were replaced using MSX Band E data, at a lower resolution than the original Spitzer data, which might underestimate the flux. The corrected 24  $\mu\text{m}$  images are not public yet.

All the data were convolved to a 37'' angular resolution to match the resolution of the Herschel 500  $\mu\text{m}$  data, with a pixel size of 13.9''. The change in resolution has been performed through convolution by a Gaussian kernel with FWHM  $\sigma_k^2 = \sigma_c^2 - \sigma_d^2$ , where  $\sigma_c$  is the common resolution, i.e. 37'', and  $\sigma_d$  is the original resolution of the data. The SPIRE 500  $\mu\text{m}$  beam profile has a plateau at  $\sim 1\%$  that extends to a radial distance of 1'. The Gaussian approximation of the beam is however valid, even for the selected annulus we consider in the following (28'' to 56', see Section 4.1).

To avoid any zero level mismatch between Herschel, Spitzer, MSX and Bolocam data, we subtract a background in all images. The background is computed as the median over a common area, corresponding to the 10% lowest values in the Bolocam data.

## 3. Two specific environments

### 3.1. UCHII regions

UCHII regions have been cataloged by Codella et al. (1994), using the association of HII regions and IRAS PSC. We choose twelve targets in the catalog, observed in both Hi-GAL and BGPS surveys, and with high 100  $\mu\text{m}$  IRAS fluxes ( $> 10^3$  Jy), to ensure studying UCHII regions that include warm dust. Because of the lower resolution of the IRAS compared to the Herschel

Regions	$F_{70}$	$F_{160}$	$F_{250}$	$F_{350}$	$F_{500}$	$F_{1100}$
IRAS 17279-3350 (1)	245.09±32.74	305.20±37.85	154.46±19.33	81.16±12.12	27.09±6.23	0.89±1.22
IRAS 17279-3350 (2)	19.24±7.47	16.65±6.25	8.31±3.65	2.72±1.11	0.78±0.46	0.06±0.03
IRAS 17455-2800 (1)	921.41±117.10	889.23±98.62	362.84±40.15	153.04±21.80	48.41±10.21	3.43±2.23
IRAS 17455-2800 (2)	31.59±16.34	35.18±15.29	26.16±9.20	12.93±4.96	4.30±1.72	0.12±0.07
IRAS 17577-2320 (1)	615.98±68.52	408.93±49.17	184.77±22.82	86.23±13.36	29.58±7.42	1.91±1.81
IRAS 17577-2320 (2)	23.21±7.66	21.64±7.89	12.38±3.86	4.58±1.53	1.91±0.59	0.11±0.05
IRAS 18032-2032 (1)	2469.66±252.86	2014.03±207.58	626.05±52.85	300.14±28.93	118.61±14.65	5.97±2.95
IRAS 18032-2032 (2)	39.31±29.51	42.27±16.37	22.11±10.21	8.26±4.07	2.44±0.82	0.11±0.04
IRAS 18116-1646 (1)	1599.22±166.58	1096.38±116.61	426.07±39.01	180.55±20.24	61.16±9.92	3.50±2.27
IRAS 18116-1646 (2)	45.06±29.29	37.45±12.57	16.82±5.32	5.93±1.70	1.69±0.65	0.10±0.04
IRAS 18317-0757 (1)	1378.92±144.14	759.41±82.87	225.24±26.13	84.00±14.14	25.89±7.51	1.77±1.78
IRAS 18317-0757 (2)	30.07±13.07	25.80±10.02	16.98±6.62	6.99±2.72	2.39±1.01	0.12±0.05
IRAS 18434-0242 (1)	3037.49±309.69	1801.52±187.72	367.84±37.81	229.12±24.56	83.98±12.58	3.59±2.58
IRAS 18434-0242 (2)	32.61±35.43	57.02±27.25	30.15±10.95	9.92±3.74	3.96±1.60	0.24±0.10
IRAS 18469-0132 (1)	720.85±78.44	646.83±70.46	311.22±28.98	148.69±16.71	53.52±8.52	2.28±1.72
IRAS 18469-0132 (2)	18.81±11.17	14.62±9.55	4.69±2.89	2.07±1.06	0.54±0.28	0.05±0.03
IRAS 18479-0005 (1)	2361.72±241.57	1581.69±163.89	495.22±42.90	282.81±26.81	92.69±12.09	5.82±2.79
IRAS 18479-0005 (2)	17.84±9.50	22.40±7.15	12.66±5.46	4.13±1.66	1.18±0.55	0.06±0.03
IRAS 18502+0051 (1)	1096.06±115.00	1076.50±113.54	472.44±41.11	235.61±23.78	80.35±11.35	2.86±2.11
IRAS 18502+0051 (2)	9.97±5.38	19.59±6.63	11.22±4.75	5.32±2.03	1.66±0.65	0.11±0.04
IRAS 19442+2427 (1)	1526.10±158.99	874.65±95.40	434.83±39.89	190.44±21.63	72.86±11.18	3.96±2.52
IRAS 19442+2427 (2)	38.06±14.83	47.92±18.29	19.69±7.66	8.57±3.61	2.34±0.95	0.15±0.08
IRAS 19446+2505 (1)	3851.74±392.29	1716.05±179.22	553.55±50.20	236.73±24.90	79.65±11.87	5.51±2.96
IRAS 19446+2505 (2)	134.00±79.70	70.81±35.01	25.71±10.49	8.00±3.13	2.87±0.77	0.17±0.08
Cold Clump-1 (1)	7.73±2.95	13.42±4.30	10.40±3.58	4.65±2.33	2.18±1.53	0.14±0.37
Cold Clump-1 (2)	0.31±0.15	0.98±0.45	0.83±0.34	0.47±0.20	0.21±0.10	0.02±0.01
Cold Clump-2 (1)	79.94±12.23	107.14±15.76	68.61±10.87	31.30±6.94	13.17±4.37	0.81±1.01
Cold Clump-2 (2)	0.37±0.31	1.47±0.77	1.55±0.63	0.73±0.28	0.34±0.14	0.02±0.01
Cold Clump-3 (1)	-	8.89±5.52	8.16±4.70	4.64±3.19	1.82±2.08	0.09±0.20
Cold Clump-3 (2)	-	1.96±0.34	1.64±0.40	0.83±0.23	0.36±0.11	0.01±0.01
Cold Clump-4 (1)	5.17±2.60	9.94±3.41	11.35±3.69	7.10±2.98	3.57±1.96	0.21±0.46
Cold Clump-4 (2)	0.20±0.08	1.28±0.24	1.30±0.33	0.79±0.31	0.27±0.12	0.02±0.01
Cold Clump-5 (1)	4.19±3.66	19.28±8.77	25.30±9.07	17.09±6.69	7.68±4.30	0.39±0.84
Cold Clump-5 (2)	0.50±0.11	2.79±1.30	3.45±1.52	2.00±0.90	0.88±0.39	0.04±0.02
Cold Clump-6 (1)	-	5.57±4.65	16.25±6.76	14.30±5.54	7.50±3.78	0.21±0.63
Cold Clump-6 (2)	-	1.18±0.49	1.77±0.85	1.01±0.66	0.46±0.32	0.03±0.02
Cold Clump-7 (1)	4.49±2.59	4.65±2.95	4.53±2.40	4.71±2.46	2.17±1.55	0.11±0.33
Cold Clump-7 (2)	0.15±0.35	2.72±0.55	2.06±0.30	0.96±0.28	0.39±0.11	0.02±0.01
Cold Clump-8 (1)	-	2.48±5.75	9.00±6.41	6.62±4.45	3.12±2.66	0.13±0.61
Cold Clump-8 (2)	-	1.80±0.36	2.22±0.56	1.33±0.32	0.58±0.15	0.03±0.01
Cold Clump-9 (1)	104.97±14.96	189.10±25.65	139.88±17.64	74.53±11.28	31.25±6.40	1.65±1.33
Cold Clump-9 (2)	0.64±0.72	6.68±2.66	6.23±2.17	3.59±1.26	1.82±0.56	0.07±0.03
Cold Clump-10 (1)	2.71±1.86	10.80±3.74	8.25±3.14	3.16±1.87	1.45±1.22	0.15±0.39
Cold Clump-10 (2)	0.88±0.22	2.39±0.42	1.63±0.30	0.80±0.14	0.31±0.06	0.02±0.01
Cold Clump-11 (1)	0.66±0.70	3.61±3.59	4.14±4.67	3.44±3.15	1.56±1.91	0.08±0.38
Cold Clump-11 (2)	-	0.75±0.21	0.97±0.39	0.42±0.16	0.20±0.09	0.01±0.01
Cold Clump-12 (1)	7.57±2.86	21.31±5.20	21.78±5.13	13.39±3.93	7.19±2.76	0.30±0.55
Cold Clump-12 (2)	0.02±0.04	0.65±0.28	0.95±0.37	0.63±0.27	0.28±0.11	0.02±0.01

**Table 2.** Fluxes (in Jy) computed in the central and surrounding part of the regions, denoted as (1) and (2).

data, the coordinates of the regions were determined by looking at the maximum of surface brightness at 160  $\mu\text{m}$ . Characteristics and images of the selected UCHII regions are given in Table 1 and Figure 1, respectively.

### 3.2. Cold clumps

We choose cold molecular clumps (previously identified from  $^{13}\text{CO}$  (observations using the BU-FCRAO Galactic Ring Survey, see Jackson et al., 2006), recently analyzed using a 3D - Galactic inversion on Herschel observations (Table 1 in Marshall et al., 2013), using HI and  $^{13}\text{CO}$  data. In this latter analysis, dust temperatures in each phase of the gas have been determined for each molecular clump. We select twelve targets that

evidence cold dust. In the following, we refer to these regions as cold clumps, even if they do not strictly correspond to the definition adopted by the Planck collaboration. However, for each cloud we look for the exact coordinates that enable us to get the maximum of surface brightness at 500  $\mu\text{m}$  (FIR/submm emission peaks do not especially correspond to HI or  $^{13}\text{CO}$  peaks). This selection leads to different coordinates compared to those in Marshall et al. (2013). Coordinates of our cold clumps selection are provided in Table 1. Images of the targets at 350  $\mu\text{m}$  are provided in Figure 2.

**Table 3.** Best-fit parameters of the TLS model derived for different environments.

Environment/parameters	$l_c$ (nm)	$A$	$c_\Lambda$	reduced $\chi^2$
Galactic diffuse*:				
Diffuse parameters	$23.05 \pm 22.70$	$9.38 \pm 1.38$	$242 \pm 123$	1.95
Galactic compact sources*:				
Compact sources parameters	$5.11 \pm 0.09$	$3.86 \pm 0.13$	$1333 \pm 68$	1.45
Galactic diffuse and compact sources*:				
Standard parameters	$13.40 \pm 1.49$	$5.81 \pm 0.09$	$475 \pm 20$	2.53
UCHII regions†:				
Diffuse parameters	$23.05 \pm 22.70$	$9.38 \pm 1.38$	$242 \pm 123$	1.27
Galactic compact sources	$5.11 \pm 0.09$	$3.86 \pm 0.13$	$1333 \pm 68$	2.09
Standard parameters	$13.40 \pm 1.49$	$5.81 \pm 0.09$	$475 \pm 20$	1.28

\* Paradis et al. (2011).

† This work.

## 4. Method

### 4.1. Aperture photometry to extract dust emission

For each UCHII region and cold clump, we intend to extract two spectral energy distributions (SEDs). It appears more reasonable to base our analysis on two SEDs per region than on only one. Instead of determining SEDs per pixels, we constructed SEDs derived from averaging several pixels. We choose the central part of the region (denoted as -(1)- in the following) which evidence bright pixels (not intended to describe the core of the region), and an annulus surrounding the central part (denoted as -(2)- in the following). In this way, we expect to obtain slight changes in dust temperature when going away from the central part, in order to sample various temperatures. For this purpose we use the *idl aper* routine to compute concentric aperture photometry. We fix the first aperture to a two pixel radius ( $27.8''$  radius), and the surrounding annulus with an inner and outer radii of two and four pixels (between  $27.8''$  and  $55.6''$ ), respectively. The SED in region (1) is background subtracted from the annulus region (2). We consider as uncertainty the quadratic sum of the uncertainty deduced from the *idl aper* routine, that includes the dispersion on the sky background (corresponding to the root mean square of the background), and the calibration uncertainty depending on each instrument. The Hi-GAL data have been generated by the ROMAGAL software (Traficante et al., 2011), which does not remove the large scale emission, as opposed to standard high-pass filtering. For these data, the calibration uncertainty has been estimated to be 10% for PACS (Poglitsch et al., 2010) and 7% for SPIRE (observer's manual v2.4). For the Bolocam data, we use 20% of calibration uncertainty, which corresponds to the comparison of the v2 version of the data with the flux from other instruments (Ginsburg et al., 2013). We note that the Bolocam data uncertainties on the output flux from the *aper* routine are large due to noise in the data. Adding a 20% calibration uncertainty, we obtain in some cases a total uncertainty twice (or even more) larger than the flux, which indicates low signal over noise ratio. We determine the flux at each wavelength from  $70 \mu\text{m}$  to  $1.1 \text{ mm}$ , to obtain FIR-mm SEDs. Flux values are provided in Table 2. We proceed in the same way to also deduce  $21.3 \mu\text{m}$  and  $24 \mu\text{m}$  fluxes in UCHII regions. SEDs are given in Figures 3 and 4.

### 4.2. Modeling

One can see in Figure 3 that fluxes in the NIR wavelengths appear to be quite high, probably due to the contribution from

small grains, stochastically heated by the radiation field. Since the models used here include a single BG component, we have to select a wavelength range where this component clearly dominates the overall emission. In addition the wavelength range is restricted by the validity of both the TLS and the T- $\beta$  models. These models are only valid in the FIR/mm, for wavelengths larger than  $\sim 50 \mu\text{m}$ , where the following assumptions can be made: the real part of the dielectric constant can be considered as constant and the size of the particules can be considered as small compared to the wavelength. Also, the  $21 \mu\text{m}$  flux in cold clumps could be biased by the absorption resulting from the silicate bands occurring at  $20 \mu\text{m}$ . Therefore, the  $21.3 \mu\text{m}$  and  $24 \mu\text{m}$  flux are not included in the modeling.

#### 4.2.1. T- $\beta$ model

The typical way to describe FIR emission is to use a simple modified black-body model, with a fixed value of  $\beta$ . The common value of  $\beta$  is 2. This type of model can be acceptable when long wavelength constraints are not available, and when looking at regions with temperatures of about 17-20 K. However there is no reason to have a unique value of  $\beta$  applicable all over the sky. Some authors claim that  $\beta$  variations are the only result of calibration uncertainties on the data, temperature mixing along the line of sight (Shetty et al., 2009) or due to applications of the  $\chi^2$  minimization technique. A Bayesian approach on the data modeling is however able to make a distinction between a real and spurious T- $\beta$  relationship (Kelly et al., 2012; Veneziani et al., 2013). Moreover, in some cases it is more than obvious that a modified black-body model with  $\beta=2$  does not work, especially in cold regions which evidence steep spectra ( $\beta \approx 3$ , see for instance Désert et al., 2008; Planck Collaboration, 2011), or hot regions with flat spectra ( $\beta \approx 1$ , see for instance Dupac et al., 2003; Kiuchi et al., 2004). However, it is not a systematic behavior. Indeed, some measurements of cold cores in the Taurus region, between  $160$  and  $2100 \mu\text{m}$ , do not show departures of  $\beta$  from  $\beta = 2$  (see for instance Schnee et al., 2010). Also, we know that the submm/mm emission varies as a function of wavelength, as observed in laboratory experiments. (Boudet et al., 2005; Coupeaud et al., 2011).

#### 4.2.2. TLS model

The TLS model is the first model that takes the physical aspect of amorphous dust material into account. We do not give here a full description of the TLS model, but we refer the reader

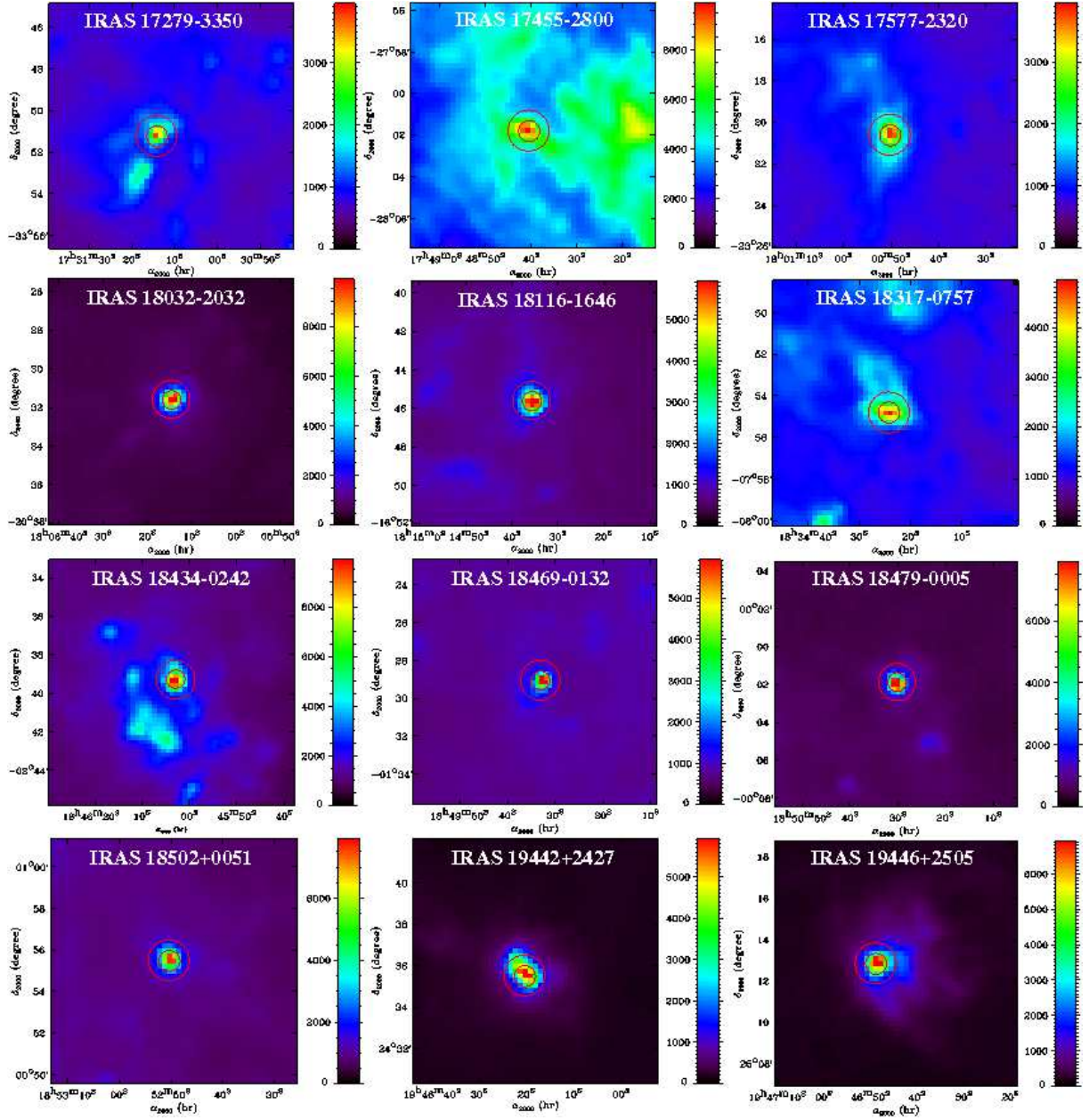


**Fig. 1.** Herschel 350  $\mu\text{m}$  images of the selected UCHII regions. The photometric apertures for which the fluxes have been computed are indicated by red circles. Central and surrounding regions are denoted (1) and (2) in the text.

to Mény et al. (2007) for a theoretical overview of the physics of the model and to Paradis et al. (2011, 2012) for comparisons of the TLS model with astrophysical data (FIRAS/WMAP, Archeops and Herschel data). In previous analyses, we looked for the best parameters allowing us to reproduce the Galactic diffuse medium (denoted as diffuse parameters or Diff.), Galactic compact sources (denoted as compact sources parameters or CS) and both environments (denoted as standard parameters or Std.). The TLS model is the combination of two distinct processes: the disordered charge distribution (DCD) part at the grain scale, and the TLS part itself, at the atomic scale. The first effect describes the interaction between the electromagnetic wave and acoustic oscillations in the disordered charge of the amorphous material (Vinogradov, 1960; Schlomann, 1964). This DCD process is characterized by a correlation length ( $l_c$ ), which controls the inflection point where two asymptotic behaviors ( $\epsilon \propto \lambda^{-2}$  and

$\epsilon \propto \lambda^{-4}$ ) occur. The TLS process takes the interaction of the electromagnetic wave with the simple distribution of an asymmetric double-well potential into account (Phillips, 1972, 1987; Anderson et al., 1972). This TLS process is characterized by three specific effects, temperature-dependent, as opposed to the DCD process. One of these TLS effects is represented by a parameter  $c_\Delta$ , that describes the tunneling states. The amplitude of the TLS effects with respect to the DCD process is controlled by a multiplying factor denoted  $A$ , i. e.  $I_{\text{tot}} = I_{\text{DCD}} + A \sum I_{\text{TLS}}$ . In the following we therefore use the three sets of parameters (Diff., CS, Std.), fixed to some specific values of  $l_c$ ,  $c_\Delta$  and  $A$  (see Table 3), derived from previous analyses (Paradis et al., 2011), when performing SED fitting with the TLS model.



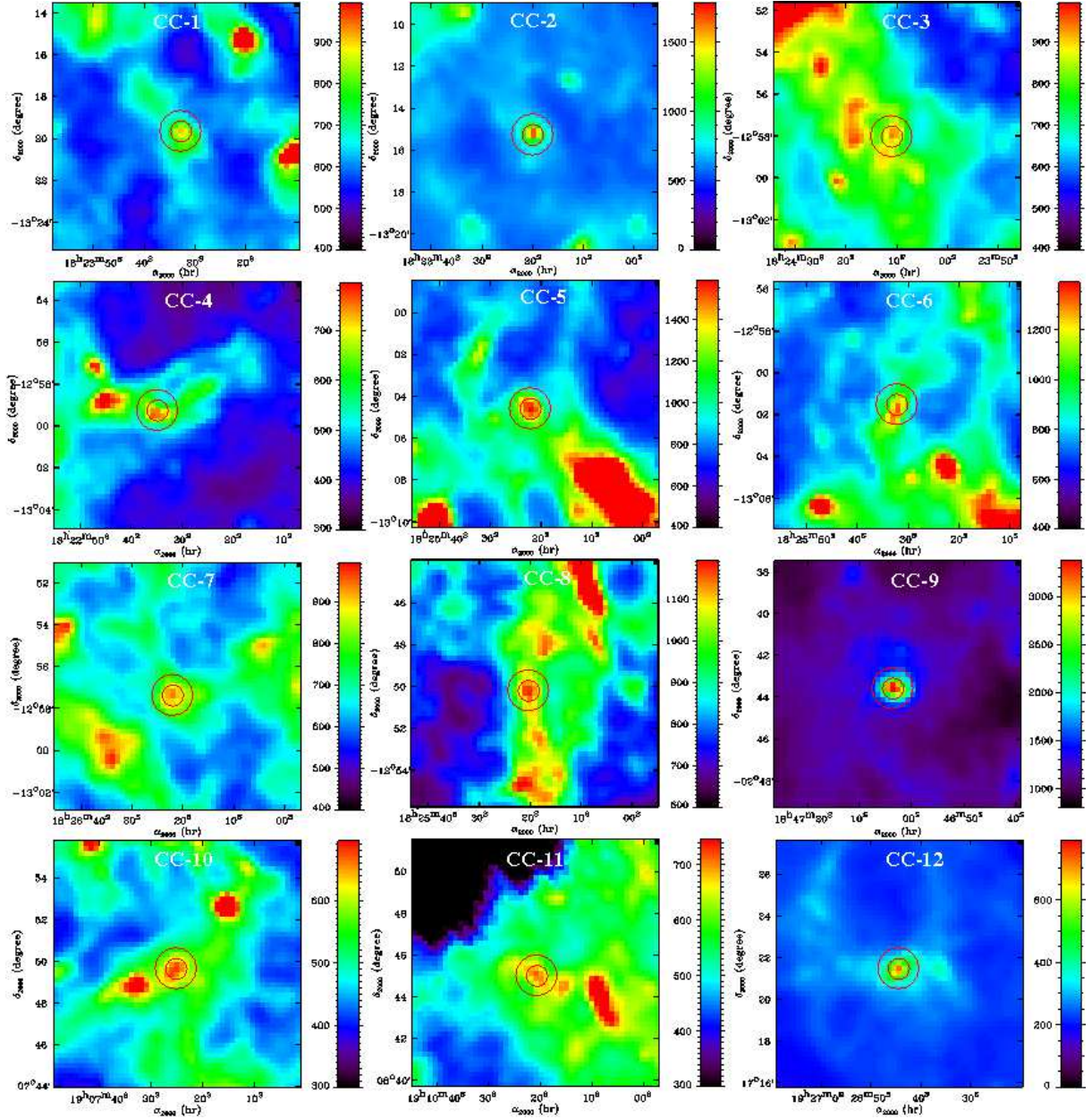


**Fig. 2.** Herschel 350  $\mu\text{m}$  images of the selected cold clump regions. The photometric apertures for which the fluxes have been computed are indicated by red circles. Central and surrounding regions are denoted (1) and (2) in the text.

#### 4.2.3. $\chi^2$ minimization

We have performed  $\chi^2$  minimizations on SEDs using both models (see Table 7). In the case of the T- $\beta$  model, we applied three values of  $\beta$  (1.5, 2 and 2.5). For the TLS model, we used the three sets of parameters defined in the previous section. The three  $\beta$  values of 1.5, 2 and 2.5 are not arbitrary values. Indeed, at first order, a mean emissivity spectral index in the submm domain derived from the TLS model is close to 2, with the use of standard parameters in the range  $\sim 17$ -25 K, 1.5 with diffuse parameters in the range  $\sim 30$ -40 K, and 2.5 with CS parameters in the range  $\sim 8$ -13 K. In that sense, the choice of these three  $\beta$  values are similar to the submm slope derived from the TLS model. However, in the TLS model, the slope in the FIR is different from the one in the submm/mm due to the DCD process in the FIR and TLS processes in the submm/mm. This change of  $\beta$  from FIR

to submm/mm has been observed in various environments (see for instance, Paradis et al., 2009; Planck Collaboration, 2014; Gordon et al., 2014). In cases of UCHII regions the  $\chi^2$  minimizations have been done between 70  $\mu\text{m}$  and 1.1 mm, whereas for cold clumps the 70  $\mu\text{m}$  flux has not been included in the fits. Indeed, for environmental temperatures higher than  $\approx 25$  K, the 70  $\mu\text{m}$  flux arises by more than 85% from big grains in equilibrium with the interstellar radiation field, based on the DustEM model (Compiègne et al., 2011). However, in cold environments, the 70  $\mu\text{m}$  emission includes a non-negligible fraction of emission coming from small grains that constantly fluctuate in temperature after a photon absorption/emission. We pre-computed brightness in the Herschel and Bolocam filters, applying the color correction associated to each instrument, using both models, for temperatures ranging from 5 to 50 K, sampled every 0.5 K. The  $\chi^2$  value was computed for each value of the grid, and

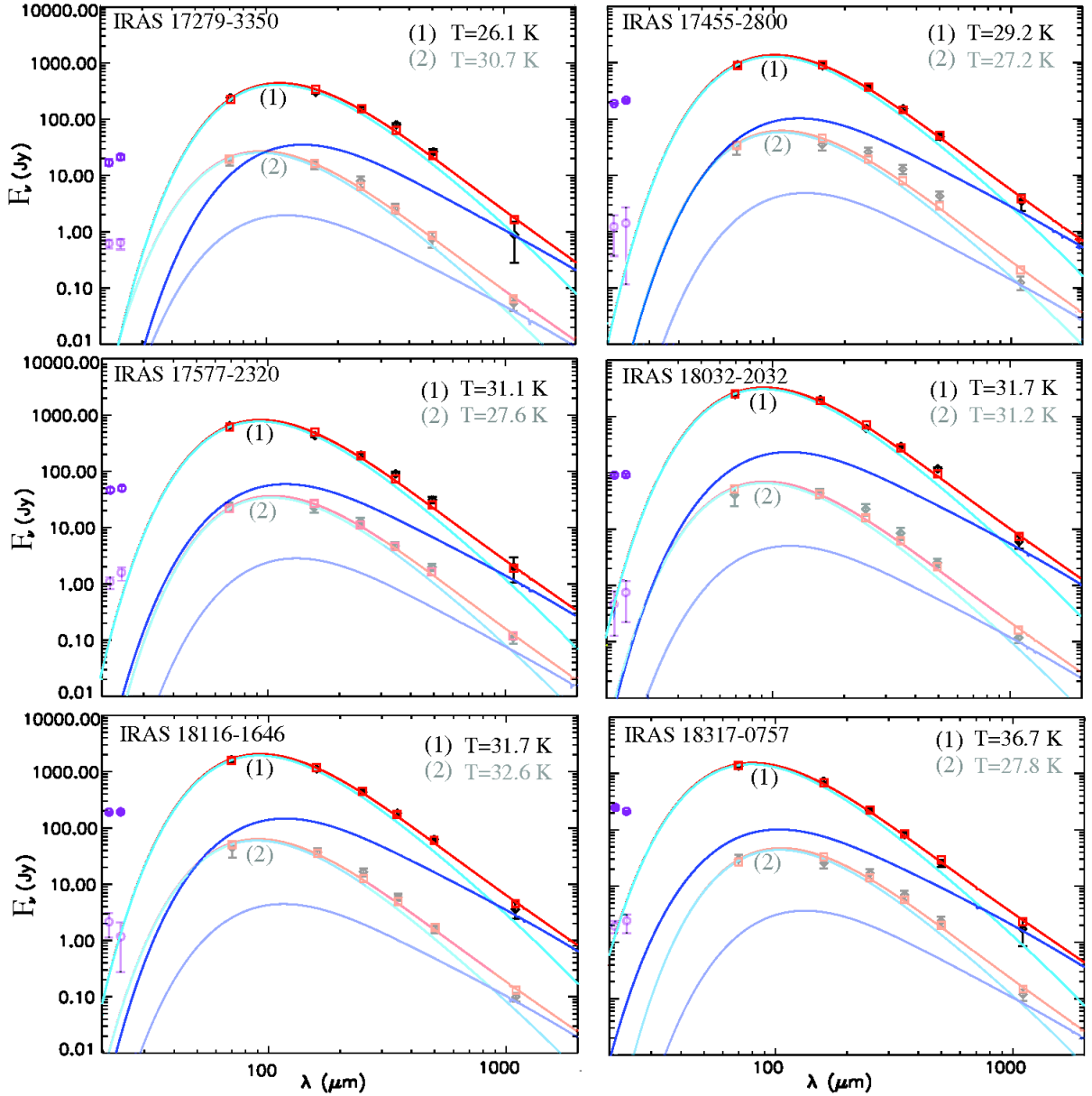


**Fig. 3.** Herschel (70, 160, 250, 350, 500  $\mu\text{m}$ ) - Bolocam (1.1 mm) SED (black diamonds) of UCHII regions, fitted with the TLS model using the diffuse parameters (total emission in red, DCD and TLS processes in light and dark blue, respectively). Squares represent models integrated in the band filters of each instrument, allowing direct comparisons with data (diamonds). SED corresponding to the central (1) and surrounding (2) part of the region are represented in regular and light colors, respectively. MSX data in band E (21.3  $\mu\text{m}$ ) and Spitzer data at 24  $\mu\text{m}$  are also visible in the plots, represented by the purple circles.

we chose the value of the dust temperature that minimizes the  $\chi^2$ . To allow interpolation between individual entries of the table, the best-fit temperature value ( $T^*$ ) is computed for the ten smallest values of  $\chi^2$  using

$$T^* = \frac{\sum_{i=1}^{10} T_i \times \frac{1}{\chi_i^2}}{\sum_{i=1}^{10} \frac{1}{\chi_i^2}}. \quad (2)$$

Temperatures derived from the fits are given in Table 4. The models were adjusted to the data by adopting the following normalization:

$$F_{model, norm}(\lambda) = \frac{F_{model}(\lambda) \times \sum_{\lambda} F_{obs}(\lambda)}{\sum_{\lambda} F_{model}(\lambda)} \quad (3)$$

where  $F_{model}$  and  $F_{model, norm}$  are the integrated flux in each band deduced from the model before and after normalization, respectively, and  $F_{obs}$  is the observational flux. The sum over the fluxes is performed between 70 and 500  $\mu\text{m}$  for SEDs of UCHII regions, and between 100 and 500  $\mu\text{m}$  for SEDs of cold clumps. We note that the dispersion in temperature values can be important from one model to the other and from one set of parameters to the other, but in that latter case the  $\chi^2$  dispersion is also large. For instance, from Table 4 one can see that with T- $\beta$  models, the mean value of temperature dispersion is 5.33 K and 3.00 K for UCHII regions and cold clumps, respectively, whereas it is of 0.38 K and 0.71 K with the TLS model. The comparison of temperatures derived from fits with the TLS model (Diffuse parameters) and T- $\beta$  model ( $\beta = 1.5$ ) with



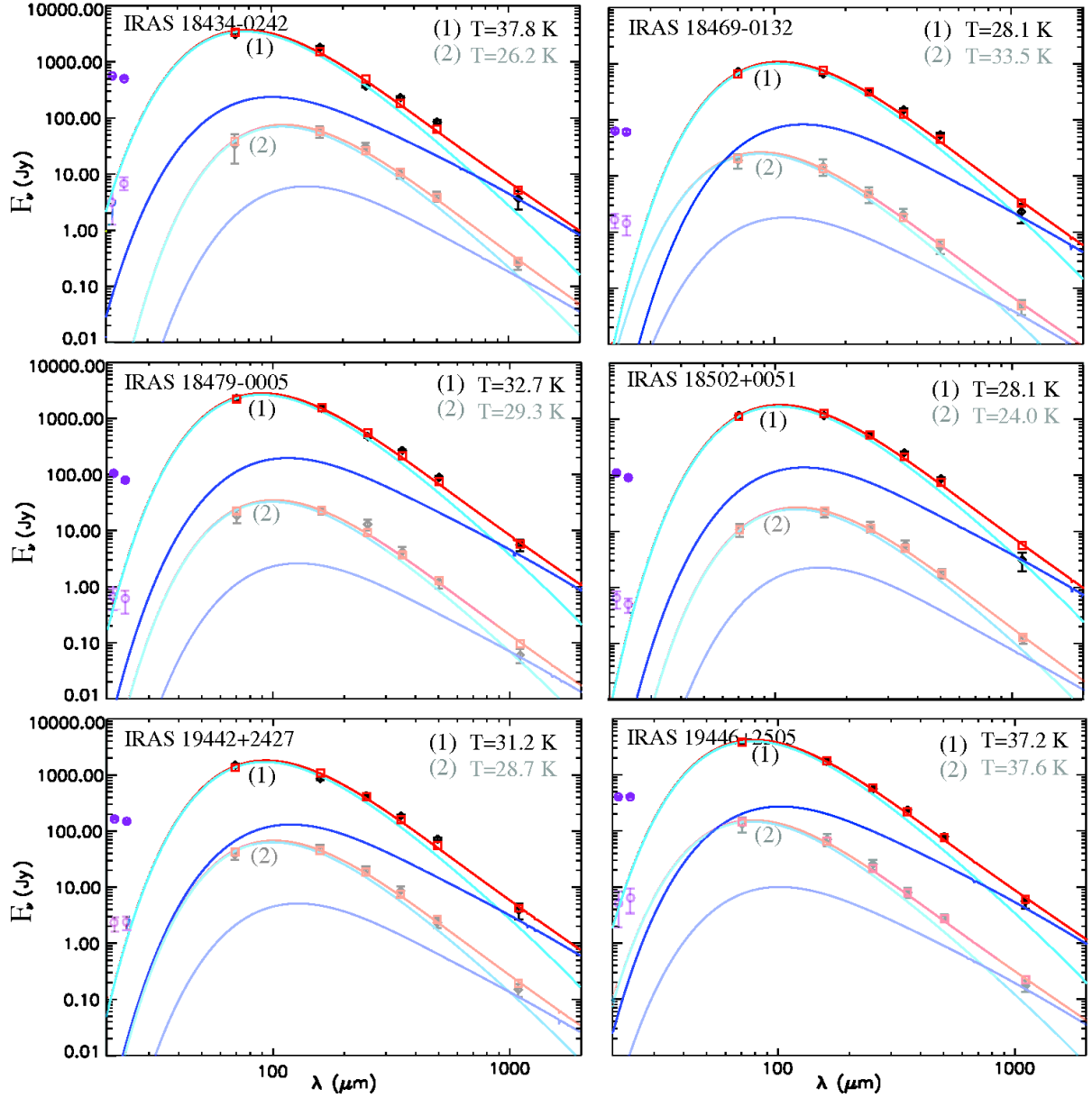


Fig. 3. Continued.

similar  $\chi^2$ , illustrates the large dispersion: 6.45 K for IRAS 18434-0242 (1) (37.76 K and 44.21 K for the TLS and T- $\beta$  model, respectively);  $\sim 5$  K for IRAS 18469-0132 (2) (33.54 K and 38.73 K, respectively) and IRAS 18032-2032 (2) (31.19 and 36.19 K, respectively). The dispersion is less important for the fitting of cold clumps (with CS parameters and  $\beta=2.5$ ): 1.71 K for CC3 (1) (15.76 K and 14.05 K); 1.61 K for CC4 (2) (15.26 K and 13.65 K); and 1.27 K for CC5 (2) (14.46 K and 13.19 K). The results show that the choice of the model has a real and important impact on the temperature determination. In the TLS model, the temperature determination is much less sensitive to the slope of the emissivity at long wavelength. This is due to the fact that, in agreement with laboratory data on silicates between 10 K and 100 K, the slope of the emissivity starts flattening with temperature in the submm range, while the temperature is mainly deduced from the FIR domain ( $\lambda < 350 \mu\text{m}$ ) in the observational data. Indeed, in the framework of the TLS model, an observed dust emissivity index far from a

value equal to 2 in the 100-350  $\mu\text{m}$  range cannot arise from intrinsic properties of silicate grains, but rather from a possible grain temperature distribution and from big grains containing carbon for instance. On the other hand, in a T- $\beta$  model, the dust emissivity index is kept constant over the whole FIR/mm range, and so in the range near the peak of emission, required for an accurate temperature determination. Therefore, for further studies on optical properties variations with environment (and temperature as a consequence), the TLS model does not present the same artefact in term of temperature determination as a T- $\beta$  model, and is especially a better description of the FIR to mm emission.

## 5. Discussion

The different trends observed between the two types of environments are deduced from the statistic made on 12 regions and the

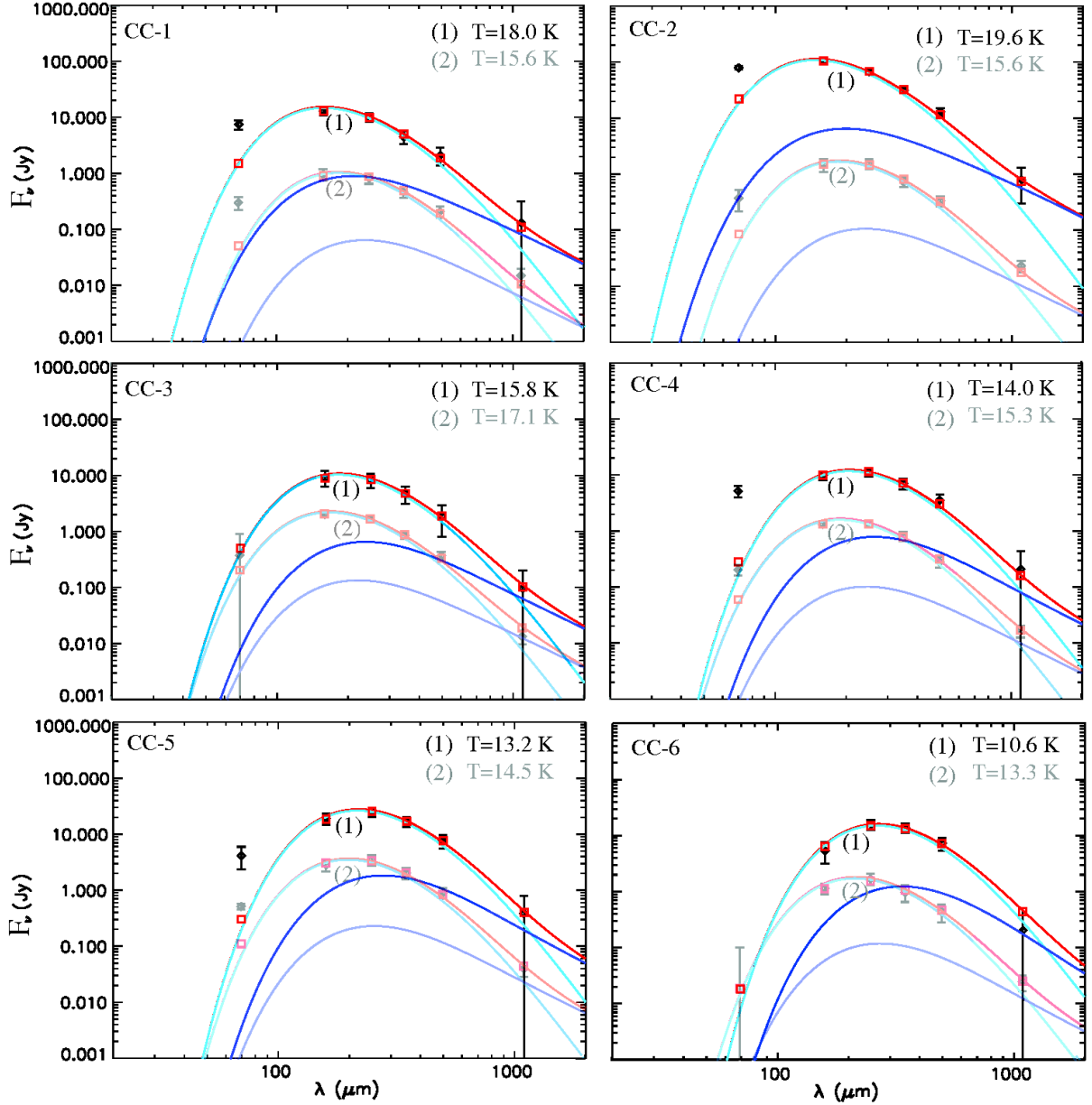


**Fig. 4.** Herschel (70, 160, 250, 350, 500  $\mu\text{m}$ ) - Bolocam (1.1 mm) SED (black diamonds) of cold clumps, fitted with the TLS model using the compact sources parameters (total emission in red, DCD and TLS processes in light and dark blue, respectively). Squares represent models integrated in the band filters of each instrument, allowing direct comparisons with data (diamonds). 70  $\mu\text{m}$  data have not been included in the fitting. SED corresponding to the central (1) and surrounding (2) part of the region are represented in regular and light colors, respectively.

analysis of 24 SEDs (since we have two SEDs per region), for each environment. We essentially focused on the total sum of the  $\chi^2$ , as well as the number of best fits (best  $\chi^2$ ) depending on the model and its associated parameters (see Table 7). In order to give the same weight to each SED we normalize the  $\chi^2$  values (Table 7), allocating the value of 1 to the largest  $\chi^2$  value derived from the TLS model, for each SED. This normalization ensures that the total  $\chi^2$  is not affected by large single  $\chi^2$  value due to a bad fit. We also normalize the  $\chi^2$  in case of T- $\beta$  modeling, keeping the same reference value. We have checked the consistency of the SED fitting results by allowing the flux density measurements to vary within the range permitted by their uncertainties. We notice although the Herschel data is internally calibrated, the zero level of the background in both PACS and

SPIRE data is not. For the Hi-GAL data, a strategy was adopted to set this background level using the IRIS and Planck calibrations (see Section 2). For the cold clumps, in particular, the entire SED wavelength range, from 160 to 500  $\mu\text{m}$ , has been cross-calibrated using the Planck data only. This allows us to have consistent flux density uncertainties, so that the spectral shape cannot be affected by the above method. We notice also that the Bolocam data has large intrinsic uncertainties, that are dominated by the noise (Bally et al., 2010), and they do not affect the SED fits, and therefore, they were not touched during the tests. For the UCHII region SEDs, the 70  $\mu\text{m}$  measurements have been cross-calibrated using a combination of IRIS and Planck calibration, so we have experimented with the uncertainties a bit more. We performed two tests; one consisting in shifting up the

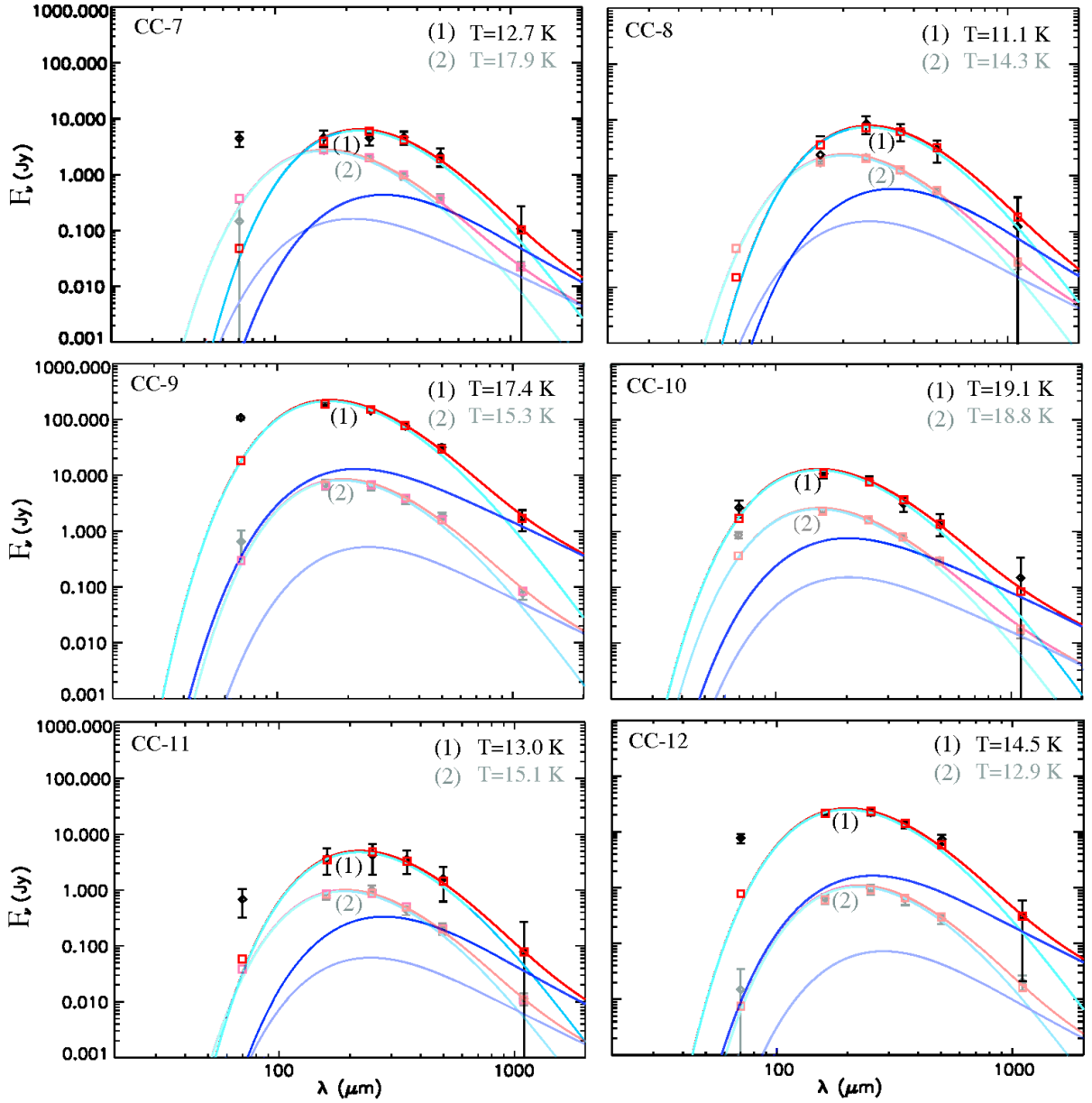


Fig. 4. Continued.

70  $\mu\text{m}$  values according to the IRIS 70  $\mu\text{m}$  derived uncertainty, and shifting down the values from 160 to 500  $\mu\text{m}$ , using the Planck uncertainties. We then performed the opposite case (shifting down the 70  $\mu\text{m}$  flux and shifting up those from 160 to 500  $\mu\text{m}$ ). For all SEDs, the best models still correspond to those identified in Table 7, i. e. we obtained similar results. Only the dust temperatures are affected by exploring the range allowed by the uncertainties, with variations of 1 to 2.5 K, depending on the SED fit.

We remind the reader that temperature mixing have not been taken into account in this analysis. This possible effect would affect both TLS and T- $\beta$  models in the same way, by inducing at first order a flattening of the spectrum. However, temperature mixing along the line of sight is expected in the inner Galactic plane. The Galactic Center, particularly exposed to such effects, showed steep spectra (Paradis et al., 2012), that goes in the opposite directions of expectations. Moreover, in Paradis et al.

(2009), the authors investigated the effect of interstellar radiation field strength mixture (as well as grain size distribution and grain composition) in cold molecular clouds, to explain steeper emissivity spectra in the FIR than in the submm/mm. They concluded that these effects could not be responsible of the submm/mm SED flattening. Even if temperature mixing could have an impact in the spectral behavior of dust emission, we do not think that this could significantly affect the conclusions of this present analysis .

### 5.1. Specific dust properties in each environment

With the TLS modeling, the total number of best fits deduced from best  $\chi^2$  indicates that compact sources (CS) parameters do not give the best description of spectra in UCHII regions (best  $\chi^2$  for only 12% of the SEDs), whereas diffuse and standard parameters give better solutions (52% and 36%, respectively). In the

Regions	Dust temperatures (K)							
	Diff.	TLS			T- $\beta$			
		CS	Std.	1- $\sigma$	$\beta=2$	$\beta=1.5$	$\beta=2.5$	1- $\sigma$
IRAS 17279-3350 (1)	26.13	25.81	25.85	0.17	25.29	29.17	22.70	3.26
IRAS 17279-3350 (2)	30.72	31.27	30.73	0.31	28.68	35.29	24.71	5.34
IRAS 17455-2800 (1)	29.17	29.17	29.12	0.03	28.21	33.21	24.76	4.25
IRAS 17455-2800 (2)	27.21	26.76	26.75	0.26	24.70	31.72	20.20	5.81
IRAS 17577-2320 (1)	31.10	31.17	30.81	0.19	30.14	35.08	26.67	4.23
IRAS 17577-2320 (2)	27.57	27.67	27.30	0.19	25.78	31.56	22.26	4.70
IRAS 18032-2032 (1)	31.67	31.80	31.66	0.08	30.29	36.22	22.61	4.85
IRAS 18032-2032 (2)	31.19	33.22	31.21	1.17	27.44	36.19	22.53	6.92
IRAS 18116-1646 (1)	31.71	32.03	31.69	0.19	30.57	36.29	26.65	4.85
IRAS 18116-1646 (2)	32.63	34.25	32.68	0.92	29.13	37.68	24.59	6.65
IRAS 18317-0757 (1)	36.65	37.27	36.69	0.35	34.92	42.66	30.03	6.37
IRAS 18317-0757 (2)	27.78	28.25	27.76	0.28	25.72	32.20	21.75	5.28
IRAS 18434-0242 (1)	37.76	38.76	38.19	0.50	36.19	44.21	30.75	6.77
IRAS 18434-0242 (2)	26.20	26.14	26.13	0.04	24.48	30.62	20.69	5.01
IRAS 18469-0132 (1)	28.14	28.15	28.11	0.02	27.21	31.69	24.16	3.79
IRAS 18469-0132 (2)	33.54	34.76	33.63	0.68	30.73	38.73	26.15	6.37
IRAS 18479-0005 (1)	32.69	33.15	32.69	0.27	31.26	37.28	27.24	5.05
IRAS 18479-0005 (2)	29.26	29.75	29.24	0.29	27.03	34.20	22.72	5.80
IRAS 18502+0051 (1)	28.10	28.10	28.06	0.02	27.14	31.72	23.77	3.99
IRAS 18502+0051 (2)	24.04	23.57	23.77	0.24	22.52	27.79	18.78	4.53
IRAS 19442+2427 (1)	31.19	31.26	31.18	0.04	30.17	35.25	26.27	4.50
IRAS 19442+2427 (2)	28.74	29.15	28.71	0.25	26.96	33.23	23.17	5.08
IRAS 19446+2505 (1)	37.20	38.23	37.27	0.58	35.24	43.23	30.20	6.57
IRAS 19446+2505 (2)	37.63	41.25	38.13	1.96	33.56	43.61	27.74	8.03
Mean std. deviation	-	-	-	0.38	-	-	-	5.33
Cold Clump-1 (1)	18.65	17.96	18.52	0.37	18.03	21.56	15.66	2.97
Cold Clump-1 (2)	16.63	15.62	16.38	0.53	15.96	19.94	13.88	3.08
Cold Clump-2 (1)	20.40	19.60	20.17	0.41	19.58	23.78	16.93	3.45
Cold Clump-2 (2)	17.01	15.58	16.59	0.74	16.21	20.64	13.80	3.47
Cold Clump-3 (1)	17.11	15.76	16.86	0.72	16.44	20.17	14.05	3.08
Cold Clump-3 (2)	19.15	17.14	18.66	1.05	18.12	23.25	15.01	4.16
Cold Clump-4 (1)	14.61	13.97	14.47	0.34	14.17	16.50	12.64	1.94
Cold Clump-4 (2)	16.98	15.26	16.52	0.89	16.12	20.18	13.65	3.29
Cold Clump-5 (1)	14.17	13.16	13.98	0.54	13.79	16.13	12.04	2.05
Cold Clump-5 (2)	17.06	14.46	16.52	1.37	16.10	20.73	13.19	3.80
Cold Clump-6 (1)	11.71	10.58	11.54	0.61	11.47	13.20	10.03	1.59
Cold Clump-6 (2)	15.19	13.30	14.89	1.02	14.59	18.18	12.24	2.99
Cold Clump-7 (1)	13.64	12.69	13.55	0.52	13.19	15.25	11.67	1.80
Cold Clump-7 (2)	19.59	17.91	19.13	0.87	18.31	24.16	15.38	4.47
Cold Clump-8 (1)	12.18	11.13	12.04	0.57	11.95	13.70	10.47	1.62
Cold Clump-8 (2)	16.56	14.25	16.04	1.21	15.67	20.16	12.99	3.62
Cold Clump-9 (1)	18.30	17.41	18.04	0.46	17.56	21.22	15.33	2.97
Cold Clump-9 (2)	17.65	15.32	17.12	1.22	16.65	21.74	13.72	4.06
Cold Clump-10 (1)	19.72	19.07	19.63	0.35	19.09	22.75	16.52	3.13
Cold Clump-10 (2)	20.53	18.82	20.10	0.89	19.15	25.17	15.96	4.68
Cold Clump-11 (1)	13.96	13.02	13.67	0.48	13.51	15.71	11.95	1.89
Cold Clump-11 (2)	16.70	15.05	16.45	0.89	16.03	20.18	13.50	3.37
Cold Clump-12 (1)	15.22	14.53	15.07	0.36	14.86	17.22	13.10	2.07
Cold Clump-12 (2)	14.09	12.90	13.79	0.62	13.56	16.55	11.76	2.42
Mean std. deviation	-	-	-	0.71	-	-	-	3.00

**Table 4.** Dust temperatures (in K) derived from the TLS and T- $\beta$  models, using different sets of parameters (diffuse, compact sources and standard parameters) and  $\beta$  values (1.5, 2 and 2.5), respectively. 1- $\sigma$  correspond to the standard deviation of dust temperature derived from the three set of TLS parameters or three  $\beta$  values. The mean values of the 1- $\sigma$  columns are also given.

case of cold clumps, this former set of parameters (CS parameters) is satisfactory for 56% of the SEDs (against 8% and 36% for diffuse and standard parameters, respectively). These results clearly point out that SEDs from UCHII regions and cold clumps are not reproduced by the same set of parameters, and therefore have different dust properties.

With the use of T- $\beta$  models, results are similar. Indeed, 62.5% of UCHII region SEDs are well reproduced using  $\beta=1.5$ ,

37.5% using  $\beta=2$ , and no SEDs are compatible with  $\beta=2.5$ . Looking at the total  $\chi^2$  value (15.5 and 24.7 for  $\beta=1.5$  and 2, respectively), it appears that the more reasonable value of  $\beta$  is 1.5. On the opposite, only 4% of cold clump SEDs have best  $\chi^2$  using a  $\beta$  of 1.5. To describe cold clumps, the number of best  $\chi^2$  are equally distributed between  $\beta=2$  and  $\beta=2.5$  (48%), and the total  $\chi^2$  is also not considerably different (14.5 and 18.0 for  $\beta=2$  and 2.5, respectively). This change in  $\beta$  (from 1.5 to 2-



**Table 5.** Results of the polynomial fit (see eq. 4) for the TLS model, for each environment.

Environment	$k_{0,i}$	$k_{1,i}$	$k_{2,i}$	$k_{3,i}$	$k_{4,i}$
Diffuse medium	3.33830	-5.36544e-3	1.65381e-6	1.63754e-11	-6.88816e-12
	-2.98801e-4	1.49526e-5	-1.42524e-7	1.41845e-12	6.72034e-13
	8.54787e-6	-2.17671e-7	1.49001e-9	1.03925e-11	-2.48183e-14
	-3.25327e-8	1.06390e-9	4.20971e-12	-1.37459e-13	2.39831e-16
	4.55497e-11	-1.10996e-12	-3.84120e-14	4.36257e-16	-6.77351e-19
Compact sources	3.34100	-6.57687e-3	1.67055e-5	-7.42107e-8	7.97846e-11
	-1.78243e-3	8.93472e-5	-1.09494e-6	3.82566e-9	-2.98224e-12
	4.27571e-5	-1.54310e-6	1.94520e-8	-5.15802e-11	2.51914e-14
	-2.53887e-7	1.06665e-8	-1.19930e-10	2.44969e-13	-2.12459e-17
	5.47140e-10	-2.43342e-11	2.47310e-13	-3.67727e-16	-2.21749e-19
Standard medium	3.33042	-5.49209e-3	2.14115e-6	-2.14173e-9	-7.90430e-12
	-2.84206e-4	1.12572e-5	-1.11099e-7	-7.48509e-11	9.32649e-13
	9.23806e-6	-1.28278e-7	1.17408e-9	1.19308e-11	-3.01610e-14
	-3.20750e-8	4.97171e-10	5.92135e-12	-1.52179e-13	2.83618e-16
	3.66206e-11	1.88461e-13	-4.33218e-14	4.82933e-16	-7.97139e-19

**Table 6.** Gaussian coefficients from Eq. 4 and 5, for the three environments.

Environment	$a_0$	$a_1$	$a_2$	$a_3$	$a_4$	$a_5$
Diffuse medium	-0.00050	0.07585	5.36111	100.19785	13.47090	499.96309
Compact sources	-0.00126	0.14795	4.52068	91.28719	9.50025	451.84591
Standard medium	-0.00062	0.09271	5.14453	90.71464	12.36827	484.87299

2.5) evidence a steepening in the long wavelength SEDs (500 - 1100  $\mu\text{m}$ ). However, possible changes in the emission spectral shape between 160  $\mu\text{m}$  and 1.1 mm is not taken into account in such a model. Therefore  $\beta$  could be higher between 160 and 500  $\mu\text{m}$ , compared to the long wavelength range (500  $\mu\text{m}$  to 1.1 mm), as already observed in Paradis et al. (2009), but would not be detected in this analysis. The opposite behavior (increase of  $\beta$  with wavelengths) would also not be visible. We do not pretend that  $\beta=1.5$  and  $\beta=2$  or 2.5 are the best values to fit spectra with respect to each environment. Indeed, slightly different values ( $\beta\sim 1.6$  for UCHII regions and  $\beta\sim 2.3$  for cold clumps) seem to better fit the SEDs. But, values of  $\beta$  equal to 1.5, 2 and 2.5 are at first order in agreement with values derived from the TLS model (see Section 4.2.3). In the same way, a better optimized set of the three TLS parameters could be obtained. Such study is out of the scope of this paper. By the way, results suggest a change in  $\beta$  with the environment.

Another important result is that CS parameters used to reproduce Archeops compact sources in our Galaxy (see Paradis et al., 2011) are also the best parameters to describe Galactic cold clumps analyzed in this work, when looking at the total number of best  $\chi^2$ . This result indicates that a same set of parameters is able to reproduce various cold sources, observed with different instruments at different wavelengths. This points out that all cold clumps have similar general properties. 52% of the SEDs of our UCHII regions can be reproduced by using the diffuse parameters when fitting with the TLS model. However, the difference with standard parameters in term of total  $\chi^2$  or number of best  $\chi^2$  is not significant. We note, that in the past, the lack of data characterizing warm environments in the FIR-mm domain, did not allow to derive TLS parameters for these regions. With dust emission SEDs in UCHII regions, we have tried to determine the best TLS parameters using the same method as in Paradis et al. (2011) when fitting the Archeops cold clumps. We performed a  $\chi^2$  minimization on the 24 SEDs of UCHII regions, with the same set of parameters (to be deter-

mined), allowing only temperature variation from one SED to another. We looked for the best set of parameters to describe our full sample of UCHII regions SEDs. The large uncertainties on the SEDs made the  $\chi^2$  minimization difficult. Indeed, large variations on the parameters had little effect on the reduced  $\chi^2$  value. For instance, the difference between the diffuse and standard parameters in the minimization of UCHII regions SEDs is small, ie. 1.27 and 1.28, respectively. We obtained a best reduced  $\chi^2$  of 1.25 with new parameters for UCHII regions, which is not significant. Moreover, the behavior of the model with these same parameters, as a function of temperature and wavelength, is similar to that using diffuse parameters. For this reason, we did not derive a new set of parameters for UCHII regions in this analysis. However, the use of CS parameters to fit UCHII regions SEDs significantly increases the reduced  $\chi^2$  value (2.09), confirming that UCHII regions have different properties compared to cold clumps. A summary of the TLS parameters characterizing various environments derived from this work and from previous analyses, is given in Table 3.

## 5.2. Comparing TLS and T- $\beta$ models

We note that the best total  $\chi^2$  for each model (TLS and T- $\beta$ ) are almost identical, whatever the environment. This means that modeling with the TLS model, using the adequate set of parameters, or a T- $\beta$  model, using the adequate  $\beta$ , are equivalent for the goodness of fit, because of the lack of strong constraints at long wavelengths, crucial to point out the divergence between the models. Concerning the TLS model, standard parameters adapt well in all cases (diffuse medium, compact sources, UCHII regions). Indeed, one can see that in term of total  $\chi^2$ , standard parameters are able to well reproduce the emission of each type of environment. This is the first model that is able to reasonably describe various types of medium with a single set of parameters, by only changing the dust temperature. In the case of a T- $\beta$  model, predictions of emission spectra in a specific environment

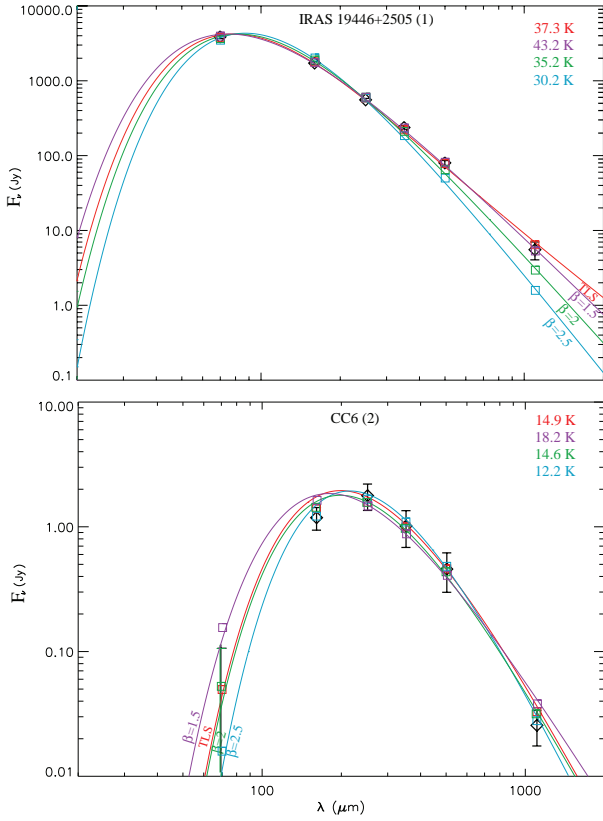


**Fig. 5.** Herschel (70, 160, 250, 350, 500  $\mu\text{m}$ ) - Bolocam (1.1 mm) SED (black diamonds) of IRAS 19446+2505 (1) and CC6 (2), fitted with the TLS model using the standard parameters in red, and with a T- $\beta$  model  $\beta=1.5$  in purple,  $\beta=2$  in green and  $\beta=2.5$  in blue. Squares represent models integrated in the band filters of each instrument, allowing direct comparisons with data (diamonds). The 70  $\mu\text{m}$  Herschel data has not been included in the fits for CC6 (2). The corresponding dust temperatures for each model are given on the top right.

require the knowledge of  $\beta$ . Otherwise, predicted emission spectra can lead to wrong descriptions (and bad  $\chi^2$ ) of dust emission in some regions.

One can see in Figure 5 two SEDs (one for an UCHII region and one for a cold clump) adjusted with the TLS model (using standard parameters) and T- $\beta$  models (using  $\beta=1.5$ ; 2; and 2.5). For IRAS 19446+2505 (1) and CC6 (2), temperatures go from 30.2 K to 43.2 K, and from 12.2 K to 18.2 K, respectively, depending on the model. Model fluxes after color-correction, ie integrated in each band filter (squares in the figure), can be directly compared to the observational SEDs (diamonds in the figure). For the cold clump, the 70  $\mu\text{m}$  flux has not been included in the fit. Whereas a T- $\beta$  model adopting a  $\beta$  value of 1.5 is able to reproduce the SED of the UCHII region, the same model gives a bad description of CC6 (2) SED, which requires a steeper spectrum ( $\beta \approx 2.5$ ). The TLS model however, describes quite well each environment, by only changing the dust temperature. The main difference between the TLS and the T- $\beta$  model with a reasonable value of  $\beta$  occurs in the mid-FIR ( $\lambda < 70 \mu\text{m}$ ) and in the mm range. But, because of the large uncertainties in the Bolocam data, especially for cold clumps where the flux can be at the same level of the noise, the 1.1 mm flux does not bring any strong constraints. However, even if in most cold clumps, removing these data from the fits give similar results, they can also help the fit

in some cases. Moreover, the 1.1 mm flux appears with the same rough estimate of what was expected, which makes us confident in the use of these data.

As a summary, each environment is characterized by a different dust emissivity index of the dust emission, indicating distinct dust properties, leading to a change in  $\beta$  in the case of a T- $\beta$  model (from  $\approx 2$ -2.5 to 1.5, corresponding to warm and cold regions), or to a change in the TLS parameters (standard, diffuse, or CS parameters), to accurately describe each type of environment. However, as opposed to a T- $\beta$  model with a fixed  $\beta$  that is not able to give good fits in warm as well as in cold regions, the use of the standard TLS parameters can reasonably reproduce all types of environment.

### 5.3. Simplifications of dust emission modeling

#### 5.3.1. Polynomial fit on the TLS model

To help the reader in using the TLS model predictions as a function of the environment, we performed a polynomial fit on the model, using the `idl sfit` function, for each set of parameters (diffuse, cold sources, and standard). This `idl` function allows us to determine a polynomial fit to a surface, which is in our case the dust absorption efficiency ( $Q_{abs}$ ) deduced from the model, as a function of temperature (6.9 K - 100 K) and wavelength (100  $\mu\text{m}$  - 2 mm). However, for temperatures between 10 K and 15 K at wavelengths around 2 mm, the difference between the model and the polynomial fit could be important. To minimize the difference we included a gaussian function in the fit (using the `idl gauss2dfit` function). The final 2D-function<sup>1</sup> used to fit the model is then given as follows:

$$\log Q_{abs}(\lambda, T) = \sum k_{j,i} \left( (\log \lambda - 2.00076) / 2.70167 \times 10^{-3} \right)^i \times \left( (T - 4.30000) / 6.46369 \times 10^{-1} \right)^j + a_0 + a_1 \times \exp\left(\frac{-U}{2}\right) \quad (4)$$

with

$$U = \left( \frac{T - a_4}{a_2} \right)^2 + \left( \frac{\lambda - a_5}{a_3} \right)^2 \quad (5)$$

The  $k_{j,i}$  and  $a$  coefficients are given in Tables 5 and 6, respectively. The wavelength range is limited to 100  $\mu\text{m}$  in the fits because in cases of cold environments, emission at wavelengths below this limit can be contaminated by emission from small grains that are not in equilibrium with the radiation field. But, since the polynomial fit is linear with wavelength in the FIR i.e. for  $\lambda < 300 \mu\text{m}$  in logarithmic scale, it can easily be extrapolated to shorter wavelengths if needed. We found that a degree of 4 is adequate to get a reasonable fit on the TLS model. Plots of the TLS model and polynomial+gaussian fits are presented in Figure 6. Predictions of dust emission derived from the TLS model (proportional to  $Q_{abs}$  values) as well as from the polynomial+gaussian fit are given in arbitrary units, which means that a normalization has to be done before using them. The reader can find reference values of emissivity or optical constants in the literature, see for instance Boulanger et al. (1996); Li & Draine (2001), that can then be converted to dust absorption efficiency. The normalization of the surface ( $Q_{abs}$ ) to a reference value at some wavelength and temperature would lead to easily determine the dust column density of any observations in the framework of the TLS model. However, reference

<sup>1</sup> IDL code available here: [http://userpages.irap.omp.eu/~dparadis/TLS/compute\\_TLS\\_poly\\_gaussian\\_fit.pro](http://userpages.irap.omp.eu/~dparadis/TLS/compute_TLS_poly_gaussian_fit.pro)

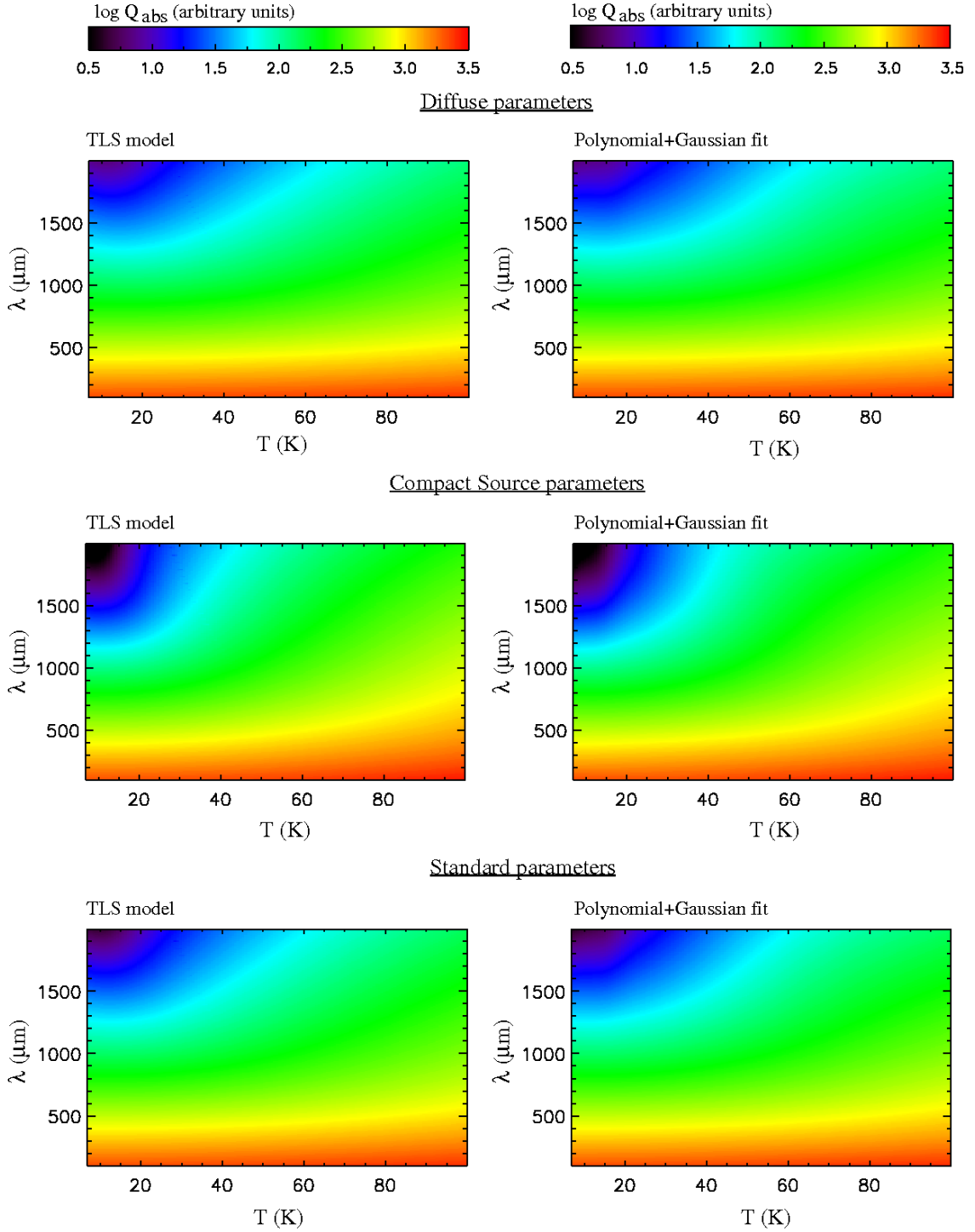


**Fig. 6.**  $\log Q_{\text{abs}}$  (in arbitrary units) as a function of temperature and wavelength derived from the TLS model (left panels) and from a Polynomial+gaussian fit performed on the TLS model (right panels), using different sets of parameters (from top to bottom: diffuse, compact sources, and standard).

values of emissivity have been determined for a given wavelength and for a specific temperature. The TLS model predicts emissivity variations as a function of wavelength and temperature. Predicted emissivities in the IRAS, Herschel and Planck bands are given in Paradis et al. (2011) for different temperatures between 5 K and 100 K. Contours of the relative error  $((Q_{\text{abs,fit}} - Q_{\text{abs,model}})/Q_{\text{abs,model}})$ , for each set of TLS parameters, are given in Figure 7. The  $1-\sigma$  standard deviation on the

relative error is 3% over the entire ranges of temperatures and wavelengths for the CS parameters, and less than 2% for the diffuse and standard parameters. For all sets of parameters, absolute errors can also reach 10-12% at low temperature ( $\sim 7$  K), in the submm and/or mm domain. We therefore encourage the user to consider only temperatures higher than 7.5 K when using the polynomial+gaussian fit. In addition, one has to be careful when using CS parameters: we note an increase in the errors

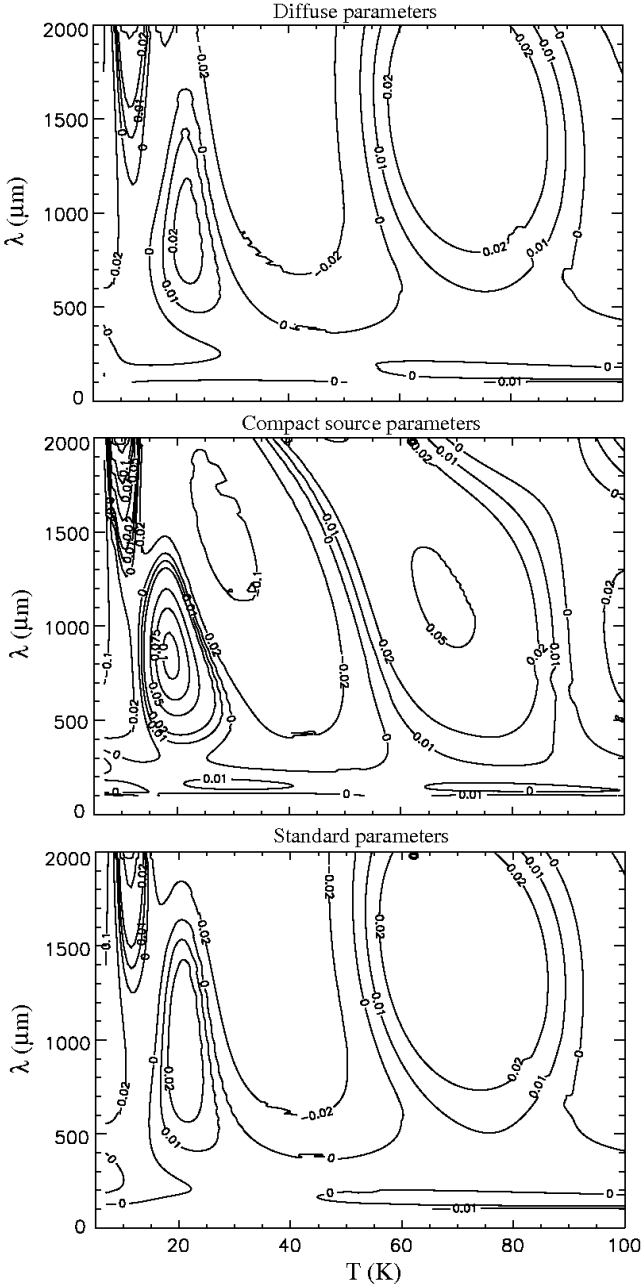


**Fig. 7.** Relative error (contours) between the polynomial+gaussian fit and the TLS model ( $(Q_{abs,fit} - Q_{abs,model})/Q_{abs,model}$ ), as a function of temperature and wavelength, for the three sets of the TLS parameters.

when reaching long wavelengths (1750-2000  $\mu\text{m}$ ), for temperatures around 10-15 K, as well as an error of 10% for wavelengths between 700  $\mu\text{m}$  and 950  $\mu\text{m}$ , and temperatures in the range 17 K - 20 K.

### 5.3.2. Universal application of the polynomial fit

The interest of the polynomial+gaussian fit is to describe dust emission SEDs between 100  $\mu\text{m}$  (or at shorter wavelengths by extrapolation when analyzing warm/hot dust grains) and 2 mm in any regions of our Galaxy. If one knows the equilibrium dust temperature then it is easy to deduce the SED. In the oppo-

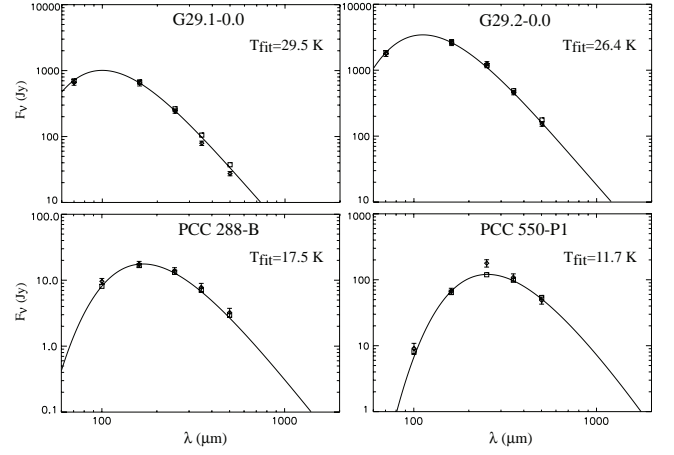


**Fig. 8.** Herschel SEDs (diamonds) of two UCHII regions G29.1-0.0 and G29.2-0.0 from Paladini et al. (2012) and two cold cores PCC 288-B and PCC 550-P1 from Juvela et al. (2010). Polynomial+gaussian fits of the TLS model are represented by continuous line between 100  $\mu\text{m}$  and 2 mm. Squares represent models integrated in the band filters of each instrument, allowing direct comparisons with data (diamonds).

site case, if one has the dust emission SED it is then possible to determine the dust temperature. To check the applicability of this polynomial+gaussian fit (performed on the TLS model with the use of the standard parameters), we compare the fit with known SEDs of UCHII regions (G29.1-0.0 and G29.2-0.0, from Paladini et al., 2012) and cold clumps (PCC 288-B and PCC 550-P1, from Juvela et al., 2010). Only the dust temperature in our fits varies from one SED to the other. Results are presented in Figure 8. As we have seen in Section 4.2.3, the determination of the dust temperature depends on the model used. Here, we did not perform any  $\chi^2$  minimization. For G29.1-0.0 and G29.2-0.0, we used temperature values of 29.5 K and 26.4 K, respectively, close to the one of the cold component (29.5 K and 25.6 K, respectively) as derived by Paladini et al. (2012) when using a two-component model with fixed dust emissivity index, to minimize SEDs between 24 and 500  $\mu\text{m}$ . In these two regions the 70  $\mu\text{m}$  emission is largely dominated by emission from the cold component. The polynomial+gaussian fits have been performed between 100  $\mu\text{m}$  and 2 mm (see Section 5.3.1), and have been extrapolated to 70  $\mu\text{m}$  here, as visible in Figure 8. For the cold clump PCC 550-P1, we considered a temperature of 11.7 K, close to the value of 11.3 K derived by Juvela et al. (2010) using a T- $\beta$  model, with a deduced  $\beta$  equal to 2.03. For PCC 288-B, the comparison between the polynomial+gaussian fit and the SED is not good when using the dust temperature derived from Juvela et al. (2010) (20.2 K), with a  $\beta$  value found equal to 1.36. With the polynomial+gaussian fit, a most appropriate value of dust temperature is around 17.5 K. We remind the reader that the fits presented in Figure 8 could be even better with the use of CC parameters in the polynomial+gaussian fits for the cold clumps, with the appropriate dust temperature. In the case of PCC 550-P1, the fit is not able to reproduce the 250  $\mu\text{m}$  flux which could be due to calibration problems that has been improved since the first Herschel data. As visible in Juvela et al. (2010), a T- $\beta$  model is also not able to match the 250  $\mu\text{m}$  flux.

We remind that model predictions essentially differ in the FIR and long wavelengths, and also lead to different dust temperatures. For this reason, we encourage the reader to use the poly-



nomial+gaussian fit (or the TLS model), which does not bias the temperature estimate, but which also takes the flattening of the spectra in the submm-mm domain into account, as opposed to  $T$ - $\beta$  models. The TLS model predicts a more correct emissivity spectral behavior than any single fixed value of  $\beta$ , and a precise description of the emissivity spectral index as a function of temperature and wavelength (see Paradis et al., 2011, Figure 6).

## 6. Conclusions

Using the combination of Herschel and Bolocam Galactic Plane surveys (Hi-GAL and BGPS), smoothed to a common resolution of  $37''$ , we analyzed dust emission associated with two specific environments : UCHII regions and cold clumps. We studied twelve regions for each environment. We extracted SEDs in the central and the surrounding part of each region. We were able to confront the recent TLS model to emission spectra from warm dust ( $\sim 30 - 40K$ ) in UCHII regions. We show that we observed some variations in the dust optical properties with environments, as revealed by the change in the dust emissivity index, or in the set of TLS parameters that best fit the emission. In addition, as opposed to any fixed value of the dust emissivity index (1.5, 2 and 2.5) that mostly fails to give good normalized  $\chi^2$  in both warm environments such as UCHII regions and cold clump regions, the use of the standard TLS parameters can give reasonable results in all cases. These standard parameters have been derived in a previous analysis to reproduce compact sources observed with Archeops as well as diffuse medium as observed with FIRAS. Using a  $T$ - $\beta$  model without the knowledge of the  $\beta$  value, can lead to a wrong description of the dust emission. This comparison shows that the TLS model can easily be used to reliably predict dust emission spectra in any regions of our Galaxy, as opposed to the  $T$ - $\beta$  model. We also give the reader, for each set of TLS parameters, an easy way to determine the emission at any temperature (in the range 7.5 K - 100 K) and wavelength (in the range  $100 \mu\text{m} - 2 \text{mm}$ ), by giving the 25 coefficients of a polynomial fit of degree 4, coupled with a gaussian fit, which accurately reproduces the BG emission, once normalized to any reference value. The IDL code of the polynomial+gaussian fit is available online.

*Acknowledgements.* This research has made use of the NASA/ IPAC Infrared Science Archive, which is operated by the Jet Propulsion Laboratory, California Institute of Technology, under contract with the National Aeronautics and Space Administration. The authors acknowledge the support of the French Agence National de la Recherche (ANR) through the program “CIMMES” (ANR-11-BS56-0029). Herschel is an ESA space observatory with science instrument provided by European-led Principal Investigator consortia and with important participation from NASA.

	Diff.	CS	Std.	Diff.	CS	Std.	$\beta = 2$	$\beta = 1.5$	$\beta = 2.5$	$\beta = 2$	$\beta = 1.5$	$\beta = 2.5$
IRAS 17279-3350 (1)	0.801	0.974	0.805	0.822	1.000	0.826	1.074	0.426	2.351	1.103	0.437	2.414
IRAS 17279-3350 (2)	0.099	0.250	0.112	0.396	1.000	0.448	0.086	0.131	0.305	0.344	0.524	1.220
IRAS 17455-2800 (1)	0.061	0.112	0.062	0.545	1.000	0.554	0.211	0.166	1.170	1.884	1.482	10.446
IRAS 17455-2800 (2)	0.842	1.158	0.847	0.727	1.000	0.731	0.477	0.886	0.581	0.412	0.765	0.502
IRAS 17577-2320 (1)	0.804	0.745	0.775	1.000	0.927	0.964	1.327	0.341	2.814	1.650	0.424	3.500
IRAS 17577-2320 (2)	0.172	0.266	0.172	0.645	1.000	0.645	0.315	0.111	0.894	1.184	0.417	3.361
IRAS 18032-2032 (1)	1.237	1.377	1.177	0.898	1.000	0.855	2.106	1.008	4.421	1.529	0.732	3.211
IRAS 18032-2032 (2)	0.408	0.911	0.448	0.448	1.000	0.492	0.049	0.373	0.191	0.054	0.409	0.210
IRAS 18116-1646 (1)	0.233	0.343	0.217	0.679	1.000	0.633	0.686	0.065	2.480	2.000	0.190	7.230
IRAS 18116-1646 (2)	0.336	0.956	0.389	0.351	1.000	0.407	0.059	0.294	0.378	0.062	0.308	0.395
IRAS 18317-0757 (1)	0.234	0.561	0.290	0.417	1.000	0.517	0.088	0.485	0.397	0.157	0.865	0.708
IRAS 18317-0757 (2)	0.288	0.443	0.291	0.650	1.000	0.657	0.296	0.239	0.741	0.668	0.539	1.673
IRAS 18434-0242 (1)	4.016	3.966	3.922	1.000	0.988	0.977	5.029	4.032	6.590	1.252	1.004	1.641
IRAS 18434-0242 (2)	0.069	0.131	0.068	0.527	1.000	0.519	0.075	0.130	0.297	0.573	0.992	2.267
IRAS 18469-0132 (1)	1.217	1.407	1.204	0.865	1.000	0.858	1.833	0.519	4.200	1.303	0.369	2.985
IRAS 18469-0132 (2)	0.041	0.118	0.048	0.347	1.000	0.407	0.100	0.066	0.250	0.847	0.559	2.119
IRAS 18479-0005 (1)	2.087	1.968	1.983	1.000	0.943	0.950	3.345	1.578	6.143	1.603	0.756	2.943
IRAS 18479-0005 (2)	0.371	0.700	0.396	0.530	1.000	0.566	0.082	0.443	0.165	0.117	0.633	0.236
IRAS 18502+0051 (1)	1.160	1.498	1.158	0.774	1.000	0.773	1.576	0.642	3.988	1.052	0.429	2.662
IRAS 18502+0051 (2)	0.052	0.073	0.050	0.712	1.000	0.684	0.096	0.136	0.483	1.315	1.863	6.616
IRAS 19442+2427 (1)	2.134	2.046	2.061	1.000	0.959	0.966	3.285	1.117	6.391	1.539	0.523	2.995
IRAS 19442+2427 (2)	0.131	0.302	0.143	0.434	1.000	0.474	0.039	0.224	0.231	0.129	0.742	0.765
IRAS 19446+2505 (1)	0.249	0.301	0.211	0.827	1.000	0.701	1.121	0.123	3.275	3.724	0.409	10.880
IRAS 19446+2505 (2)	0.111	0.512	0.151	0.217	1.000	0.295	0.091	0.055	0.386	0.178	0.107	0.754
Total nb. of best $\chi^2$	-	-	-	13 (52%)	3 (12%)	9 (36%)	-	-	-	9 (37.5%)	15 (62.5%)	0 (0%)
Total $\chi^2$	-	-	-	15.811	23.817	15.899	-	-	-	24.679	15.478	71.733
Cold Clump-1 (1)	0.017	0.021	0.017	0.810	1.000	0.810	0.017	0.027	0.026	0.810	1.286	1.238
Cold Clump-1 (2)	0.002	0.068	0.008	0.029	1.000	0.117	0.011	0.030	0.088	0.162	0.441	1.294
Cold Clump-2 (1)	0.019	0.036	0.015	0.528	1.000	0.417	0.021	0.047	0.101	0.583	1.306	2.806
Cold Clump-2 (2)	0.037	0.104	0.031	0.356	1.000	0.298	0.030	0.115	0.121	0.288	1.106	1.163
Cold Clump-3 (1)	0.014	0.001	0.009	1.000	0.071	0.643	0.008	0.045	0.001	0.571	3.214	0.071
Cold Clump-3 (2)	0.551	0.170	0.441	1.000	0.301	0.800	0.305	1.045	0.062	0.553	1.897	0.113
Cold Clump-4 (1)	0.007	0.023	0.006	0.304	1.000	0.261	0.008	0.029	0.023	0.348	1.261	1.000
Cold Clump-4 (2)	0.255	0.022	0.185	1.000	0.086	0.725	0.147	0.701	0.021	0.576	2.749	0.082
Cold Clump-5 (1)	0.028	0.003	0.019	1.000	0.107	0.679	0.020	0.090	0.003	0.714	3.214	0.107
Cold Clump-5 (2)	0.270	0.026	0.200	1.000	0.096	0.741	0.188	0.556	0.023	0.696	2.059	0.085
Cold Clump-6 (1)	0.243	0.056	0.200	1.000	0.230	0.823	0.216	0.427	0.098	0.889	1.757	0.403
Cold Clump-6 (2)	0.169	0.015	0.114	1.000	0.089	0.675	0.121	0.422	0.014	0.716	2.497	0.083
Cold Clump-7 (1)	0.099	0.119	0.097	0.832	1.000	0.815	0.103	0.103	0.128	0.866	0.866	1.076
Cold Clump-7 (2)	0.121	0.025	0.076	1.000	0.207	0.628	0.030	0.438	0.188	0.248	3.620	1.554
Cold Clump-8 (1)	0.066	0.027	0.058	1.000	0.409	0.879	0.058	0.106	0.033	0.879	1.606	0.500
Cold Clump-8 (2)	0.932	0.055	0.679	1.000	0.059	0.729	0.639	2.028	0.080	0.686	2.176	0.086
Cold Clump-9 (1)	0.049	0.102	0.033	0.480	1.000	0.324	0.033	0.166	0.184	0.323	1.627	1.804
Cold Clump-9 (2)	0.351	0.100	0.266	1.000	0.285	0.758	0.238	0.658	0.100	0.678	1.875	0.285
Cold Clump-10 (1)	0.042	0.040	0.042	1.000	0.952	1.000	0.042	0.052	0.043	1.000	1.238	1.024
Cold Clump-10 (2)	0.254	0.071	0.189	1.000	0.280	0.744	0.053	0.604	0.088	0.209	2.378	0.346
Cold Clump-11 (1)	0.010	0.008	0.007	1.000	0.800	0.700	0.009	0.018	0.009	0.900	1.800	0.900
Cold Clump-11 (2)	0.264	0.099	0.203	1.000	0.375	0.769	0.189	0.595	0.095	0.716	2.254	0.360
Cold Clump-12 (1)	0.064	0.094	0.056	0.681	1.000	0.596	0.065	0.111	0.103	0.691	1.181	1.100
Cold Clump-12 (2)	0.039	0.055	0.024	0.710	1.000	0.436	0.022	0.180	0.027	0.400	3.273	0.490
Total nb. of best $\chi^2$	-	-	-	2 (8%)	14 (56%)	9 (36%)	-	-	-	12 (48%)	1 (4%)	12 (48%)
Total $\chi^2$	-	-	-	19.730	13.347	15.367	-	-	-	14.502	46.681	17.970

**Table 7.** Reduced  $\chi^2$  derived from fits between Herschel-Bolocam data and TLS and T- $\beta$  modeling, using different sets of parameters (diffuse, compact sources and standard parameters, columns 2, 3 and 4, respectively) and  $\beta$  values (2, 1.5 and 2.5, columns 8, 9 and 10). Values of reduced  $\chi^2$  presented in columns 5, 6, 7 and 11, 12, 13 are normalized with respect to the largest  $\chi^2$  value derived from the TLS model.

## References

- Anderson, P. W., Halperin, B. I., & Varma, C. M. 1972, *Phil. Mag.*, 25, 1
- Aguirre, J. E., Ginsburg, A. G., Dunham, M. K., et al. 2011, *ApJS*, 192, 4
- Bally, J., Aguirre, J., Battersby, C., et al. 2010, *ApJ*, 721, 137
- Bernard, J.-P., Paradis, D., Marshall, D. J. 2010, *A&A*, 581L, 88
- Boudet, N., Mutschke, H., Nayral, C., et al. 2005, *ApJ*, 633, 272
- Boulanger, F., Abergel, A., Bernard, J.-P., et al. 1996, *A&A*, 312, 256
- Carey, S. J., Noriega-Crespo, A., Mizuno, D. R., et al. 2009, *PASP*, 121, 76
- Codella, C., Felli, M. & Natale, V. 1994, *A&A*, 284, 233
- Compiègne, M., Verstrete, L., Jones, A., et al. 2011, *A&A*, 525, 103
- Coupeaud, A., Demyk, K., Mény, C., et al. 2011, *A&A*, 535, 124
- Désert, F.-X., Macías-Pérez, J. F., Mayet, F., et al. 2008, *A&A*, 481, 411
- Draine, B. T. & Lee, H. M. 1984, *ApJ*, 285, 89
- Dupac, X., Bernard, J.-Ph., Boudet, N., et al. 2003, *A&A*, 404, L11
- Finkbeiner, D. P., Davis, M., & Schlegel, D. J. 1999, *ApJ*, 524, 867
- Galliano, F., Madden, S. C., Jones, A., et al. 2005, *A&A*, 434, 867
- Galliano, F., Hony, S., Bernard, J.-P., et al. 2011, *A&A*, 536, 88
- Ginsburg, A., Glenn, J., Rosolowsky, E., et al. 2013, *ApJS*, 208, 14
- Gordon, K., Galliano, F., Hony, S., et al. 2010, *A&A*, 518L, 89
- Gordon, K., Roman-Duval, J., Bot, C., et al. 2014, *arXiv1406.7469*
- Jackson, J. M., Rathborne, J. M., Shah, R. Y., et al. 2006, *ApJS*, 163, 145
- Juvela, M., Ristorcelli, I., Montier, L., et al. 2010, *A&A*, 518, L93
- Juvela, M., Montillaud, J., Ysard, N., & Lunttila, T. 2013, *A&A*, 556, 63
- Kelly, B. C., Shetty, R., Stutz, A. M., et al. 2012, *ApJ*, 752, 55
- Kiuchi, G., Ohta, K., Sawicki, M., & Allen, M. 2004, *AJ*, 128, 2743
- Kohler, M., Guillet, V., & Jones, A. 2011, *A&A*, 528, 96
- Kohler, M., Stepnik, B., Jones, A., et al. 2012, *A&A*, 548, 61
- Li, A., & Draine, B. 2001, *ApJ*, 554, 778
- Marshall, D. J., et al. 2013, *A&A*, in prep.
- Mennella, V., Brucato, J. R., Colangeli, L., et al. 1998, *ApJ*, 496, 1058
- Mény, C., Gromov, V., Boudet, N., et al. 2007, *A&A*, 468, 171
- Miville-Deschênes, M. A., & Lagache, G. 2005, *ApJS*, 157, 302
- Molinari, S., Swinyard, B., Bally, J., et al. 2010a, *PASP*, 122, 314
- Molinari, S., Swinyard, B., Bally, J., et al. 2010b, *A&A*, 518, 100
- Paladini, R., Montier, L., Giard, M., et al. 2007, *A&A*, 465, 839
- Paladini, R., Umama, G., Veneziani, M., et al. 2012, *ApJ*, 760, 149
- Paradis, D., Bernard, J.-P. & Mény, C. 2009, *A&A*, 506, 745
- Paradis, D., Veneziani, M., Noriega-Crespo, A., et al. 2010, *A&A*, 520, L8
- Paradis, D., Bernard, J.-P., Mény, C., & Gromov, V. 2011, *A & A*, 534, 118
- Paradis, D., Paladini, R., Noriega-Crespo, A., et al. 2012, *A&A*, 537, 113
- Peeters, E., Martin-Hernandez, N. L., Damour, F., et al. 2002, *A&A*, 381, 571
- Phillips, W. 1972, *J. Low Temp. Phys.*, 11, 757
- Phillips, W. 1987, *Rep. Prog. Phys.*, 50, 1657
- Planck Collaboration 2011, *A&A*, 536, 23
- Planck Collaboration 2014, *A&A*, 564, 45
- Poglitsch, A., Waelkens, C., Geis, N., et al. 2010, *A&A*, 518, 2
- Reach, W.T., Dwek, E., Fixsen, D.J., & Hewagama, T. et al., 1995, *ApJ*, 451, 188
- Schlomann, E. 1964, *Phys. Rev.*, 135, 413
- Schnee, S., Enoch, M., Noriega-Crespo, A., et al. 2010, *ApJ*, 708, 127
- Shetty, R., Kauffmann, J., Schnee, S., et al. 2009, *ApJ*, 696, 2234
- Stepnik, B., Abergel, A., Bernard, J.-P., et al. 2003, *A&A*, 398, 551
- Traficante, A., Calzoletti, L., Veneziani, M., et al. 2011, *MNRAS*, 416, 2932
- Veneziani, M., Ade, P. A. R., Bock, J. J., et al. *ApJ*, 2010, 713, 959
- Veneziani, M., Piacentini, F., Noriega-Crespo, A., et al. *ApJ*, 2013, 772, 56
- Vinogradov, V. S. 1960, *Fiz. Tverd. Tela*, 2, 2622 (English transl. 1961, *Sov. Phys. Solid St.* 2, 2338)
- Wood, D. O. S., & Churchwell, E. 1989a, *ApJ*, 340, 265
- Wood, D. O. S., & Churchwell, E. 1989b, *ApJS*, 69, 831